

Neutrino and electromagnetic signatures from Superluminous Supernovae: a case study for SN 2017egm

MAINAK MUKHOPADHYAY ^{1,2} SHIGEO S. KIMURA ³ INDREK VURM ⁴ AND BRIAN D. METZGER ^{5,6}

¹*Astrophysics Theory Department, Theory Division, Fermi National Accelerator Laboratory, Batavia, Illinois 60510, USA**

²*Kavli Institute for Cosmological Physics, University of Chicago, Chicago, Illinois 60637, USA*

³*Frontier Research Institute for Interdisciplinary Sciences; Astronomical Institute, Graduate School of Science, Tohoku University, Sendai 980-8578, Japan*

⁴*Tartu Observatory, University of Tartu, Tõravere, 61602 Tartumaa, Estonia*

⁵*Department of Physics and Columbia Astrophysics Laboratory, Columbia University, New York, NY 10027, USA*

⁶*Center for Computational Astrophysics, Flatiron Institute, 162 5th Ave, New York, NY 10010, USA*

ABSTRACT

Superluminous supernovae (SLSNe) are rare transients that are $\sim 10-100$ times more luminous than ordinary stellar explosions, reaching peak optical luminosities $\sim 10^{44}-10^{45}$ erg s⁻¹. The energy source powering SLSNe remains uncertain. In this work, we explore the multi-wavelength and multi-messenger signatures of the scenario in which SLSNe are powered by a newly born millisecond magnetar. We model the dynamical evolution and emission from the coupled system comprised of the magnetar, wind, nebula, and supernova ejecta, consistently evaluating the pair multiplicity of the wind and nebula regions, and the bulk wind Lorentz factor governing the $e^+ - e^-$ injection spectra in the nebula. We compute the thermal and non-thermal electromagnetic signatures, neutrino signatures, and investigate their detection prospects. For SN 2017egm, the nearest observed SLSNe, our prediction for high-energy gamma rays matches the recent detection by Fermi LAT. For neutrinos, using SN 2017egm a canonical SLSNe, we find that in the era of the Vera C. Rubin Observatory, a stacking analysis with upcoming neutrino observatories can lead to 3σ detection significance of neutrino events from a population of SLSNe within a decade of operation.

1. INTRODUCTION

The Vera C. Rubin Observatory Legacy Survey of Space and Time (LSST) (Ž. Ivezić et al. 2019; B. Blum et al. 2022) will detect roughly $\mathcal{O}(10^4)$ superluminous supernovae (SLSNe) every year (see T. J. Moriya 2024 for a review). These comparatively rare, but bright optical transients achieve peak absolute magnitudes $M_{AB} \gtrsim -21$ (A. Gal-Yam 2019), making them a few 10 – 100 times brighter than ordinary supernovae (SNe) resulting from the core-collapse of massive stars. Since the first confirmed observation of the superluminous SN2005ap (R. M. Quimby et al. 2007), roughly twenty years ago, a large sample of SLSNe have been discovered, leading to a population of these transients (see Z. H. Chen et al. 2023, S. Gomez et al. 2024 for recent compilations). Moreover, spectroscopic characterizations have revealed distinct hydrogen poor (Type

I; R. M. Quimby et al. 2011) and hydrogen-rich (Type II; N. Smith et al. 2010) sub-populations for SLSNe. However, even with this growing and diverse population, and optimistic future detection prospects by the LSST, a clear theory for the origin of SLSNe remains elusive.

Several theories have been proposed for the power source behind SLSNe. One model postulates they arise from shock interaction between supernova ejecta with a surrounding dense (optically-thick) circumstellar medium (CSM), leading to reprocessed interaction-powered emission (E. O. Ofek et al. 2007; R. M. Quimby et al. 2011; K. Murase et al. 2011; R. A. Chevalier & C. M. Irwin 2011), offering a particularly compelling explanation for many Type-II SLSNe. Another possible origin for SLSNe are pair-instability SNe and their associated large yield of radioactive ⁵⁶Ni (A. Gal-Yam et al. 2009; A. Gal-Yam & D. C. Leonard 2009). A newly-born millisecond magnetar, that is, the compact remnant left over following the core-collapse of the rapidly spinning star, were also proposed to power SLSNe (D. Kasen & L. Bildsten 2010; S. E. Woosley 2010; L. Dessart

Corresponding author: Mainak Mukhopadhyay
mainak@fnal.gov

* FERMILAB-PUB-26-0187-T

et al. 2012; K. Kotera et al. 2013; B. D. Metzger et al. 2014; K. Murase et al. 2015; A. Suzuki & K. Maeda 2017; B. D. Metzger et al. 2017; B. Margalit et al. 2018; C. M. B. Omand & N. Sarin 2023; J.-P. Zhu et al. 2024). The magnetar model is particularly relevant for H-poor Type-I SLSNe lacking obvious evidence for CSM interaction and will be the main focus of this work.

Given the uncertainties regarding what powers SLSNe, multi-messenger signatures, in particular, electromagnetic (EM) and neutrino signatures offer complementary probes of the potential existence of a central engine in a given SLSN, or for a population of SLSNe. For example, interaction- and magnetar-powered SLSNe can produce high-energy gamma-rays and neutrinos in the GeV-TeV range (B. Katz et al. 2012; K. Murase et al. 2014; K. Murase 2024; K. Murase et al. 2016; K. Fang & B. D. Metzger 2017; K. Fang et al. 2019; K. Murase et al. 2021; T. Eftekhari et al. 2021) as a result of particle acceleration in the environment surrounding the explosion. However, until recently, dedicated point source searches and stacking studies (N. Renault-Tinacci et al. 2018) for high-energy gamma rays using Fermi Large Area Telescope (LAT) data, did not yield a significant detection. The situation for neutrino searches also remains similar (A. Kheirandish & K. Murase 2023; T. Pitik et al. 2023; R. Abbasi et al. 2023) with no significant detection of signal events.

Our results are timely for several reasons. The recent detection of GeV emission from the nearest SLSNe SN 2017egm (S. Li et al. 2024), is consistent with existing predictions of a magnetar engine for SLSNe (I. Vurm & B. D. Metzger 2021). As we shall show, our model calibrated using magnetar and ejecta parameters matched to the optical observations of SN 2017egm, consistently reproduces the observed GeV emission by Fermi LAT (see bottom panel of Figure 1). In the future, upcoming EM surveys including Rubin LSST will build a large catalog of SLSNe spanning multiple wavelengths. It will then become possible to perform stacking searches for high-energy neutrinos using spatial, temporal, and energy dependent likelihood techniques, which constrain the physical parameters of the magnetar model.

This brings us to the central question addressed in this *Letter* – What are the multi-wavelength electromagnetic and neutrino observational prospects for magnetar-powered SLSNe? To answer this, we develop several novel aspects in the current work. We consistently follow the injection of particles and rotational energy from the magnetar into the surrounding environment, and then solve for the leptonic and hadronic cascades and interactions resulting in thermal and non-thermal photons and neutrinos *both* in the nebula (dominated by

$p\gamma$) and in the ejecta (dominated by pp). This allows us to investigate the observational prospects across the EM spectrum and for high-energy neutrinos with current and upcoming EM and neutrino telescopes, respectively. For the first time, we systematically evaluate the pair multiplicity in the wind and nebula regions and estimate the bulk Lorentz factor of the wind, where the latter governs the pair injection spectra in the nebula and subsequently the observational signatures.

The *Letter* is organized as follows. In Section 2 we compare the results from our model and observational data for SN 2017egm to choose our fiducial parameters. We discuss our model of magnetar driven SLSNe including the ejecta properties in Section 3. The resulting observational neutrino and EM signatures are presented in Section 4. We conclude and discuss the implications of our work in Section 5. Additional details are provided in Appendices A, B, C, and D.

2. OBSERVATIONAL MOTIVATIONS: SN 2017egm

Over the past two decades several hundred SLSNe have been discovered (R. M. Quimby et al. 2007; S. Gomez et al. 2024), including several with multi-wavelength observations. Amongst this observed sample, SN 2017egm is the nearest hydrogen-poor SLSNe, with a luminosity distance $d_L \approx 135$ Mpc ($z = 0.0307$). In this section we use optical data on SN 2017egm to motivate the magnetar and ejecta parameters of the canonical model adopted in this work.

SN 2017egm was discovered on May 23, 2017, by the Gaia satellite (Gaia 17biu; A. Delgado et al. 2017). Radio (S. Bose et al. 2018) and X-ray observations (0.5 - 10 keV bands) (D. N. Burrows et al. 2005) did not result in detections but instead placed constraining upper limits on the emission escaping the system at these energies. Most of the radiation from SLSNe occurs in the UV/optical bands, with J. Zhu et al. (2023) presenting a comprehensive photometric and spectroscopic survey of SN 2017egm. From this reference we obtain the the observed bolometric luminosity ($L_{\text{bol}} = E_{\text{th}}/t_{\text{diff}}^{\text{ej}}$, where E_{th} is the energy in thermal photons and $t_{\text{diff}}^{\text{ej}}$ is the diffusion time of the photons through the ejecta) and thermal temperature (T_{th}). The observed data for L_{bol} (dark green circles) and T_{th} (dark yellow circles) is shown in Figure 1 in the *top* and *middle* panels respectively. Predictions for L_{bol} and T_{th} from the magnetar model described in this work, are shown as light purple and green lines in the *top* and *middle* panels of Figure 1, respectively.

The bolometric luminosity of the model matches reasonably well with the light-curve data within $t - t_{\text{pk}} \sim 50$ days, where the optical peak occurs at $t = t_{\text{pk}}$. The

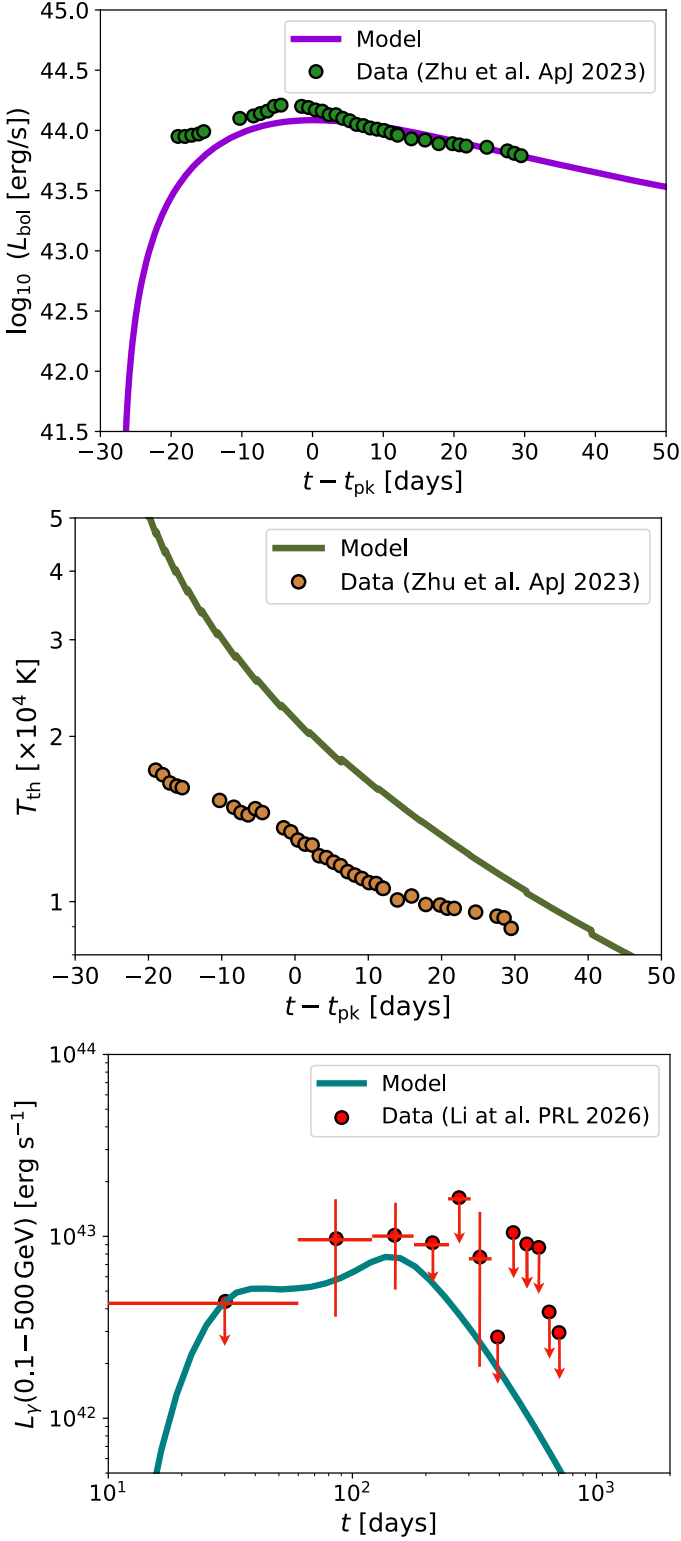


Figure 1. Model predictions (solid lines) and observational data (filled circles) for SN 2017egm. The *top* panel shows the time evolution of the bolometric luminosity (L_{bol}), the *middle* panel shows the evolution of the thermal temperature (T_{th}), and the *bottom* panel shows the evolution of the light curve in 0.1 – 500 GeV band. The time at which L_{bol} peaks is defined as t_{pk} while t denotes the time elapsed since the onset of the supernova.

thermal temperature evolution of the model differs most significantly (by a factor of ~ 2) at early times $t \lesssim t_{\text{pk}}$; however, such differences are to be expected because we employ a simplified one-zone model for the ejecta and that does not accurately track the location of its photosphere. For purposes of motivating the ejecta and magnetar properties needed to fit SN 2017egm, this level of agreement is sufficient. Remarkably, we shall show that our model with these same chosen parameters, fit to the evolution of L_{bol} and T_{th} , predict GeV emission consistent with that observed from SN 2017egm by Fermi LAT (S. Li et al. 2024), as shown in the *bottom* panel of Figure 1.

3. MODEL

Our model for SLSNe is similar to that developed and described in detail in M. Mukhopadhyay et al. (2025); M. Mukhopadhyay & S. S. Kimura (2025) for long-lived magnetar remnants from binary neutron star mergers. In this section we shall therefore focus on the most relevant aspects of the model and highlight those parts that differ from our previous works.

The core-collapse of a rapidly spinning star leaves behind a remnant neutron star characterized by a millisecond initial spin period ($P_i \sim 1 - 5$ ms) and a strong dipolar magnetic field of strength $B_d \sim 10^{13} - 10^{15}$ G. This remnant is defined as a *magnetar*. The magnetar loses its spin energy due to magnetically-driven (pulsar-like) winds. This energy resulting from the spinning down of the pulsar, also known as the spindown energy, is deposited behind an expanding ejecta and leads to the formation of a hot nebula. The magnetar’s spindown energy acts as the reservoir for the thermal (E_{th}), non-thermal (E_{nth}), magnetic (E_B), and kinetic energy via PdV work done on the system. The dynamics of the system is solved by evolving these energies (M. Mukhopadhyay et al. 2025; M. Mukhopadhyay & S. S. Kimura 2025, 2026) using the following equations (see also B. D. Metzger & A. L. Piro 2014)

$$\frac{dE_{\text{nth}}}{dt} = L_{\text{sd}} - \frac{E_{\text{nth}}}{R} \frac{dR}{dt} - \frac{E_{\text{nth}}}{t_{\text{diff}}^{\text{neb}}}, \quad (1)$$

$$\frac{dE_{\text{th}}}{dt} = (1 - \mathcal{A}) \frac{E_{\text{nth}}}{t_{\text{diff}}^{\text{neb}}} - \frac{E_{\text{th}}}{R} \frac{dR}{dt} - \frac{E_{\text{th}}}{t_{\text{diff}}^{\text{ej}}} + Q_{\text{Ni}}^{\text{heat}}, \quad (2)$$

$$\frac{dE_B}{dt} = \varepsilon_B L_{\text{sd}} - \frac{E_B}{R} \frac{dR}{dt}, \quad (3)$$

where L_{sd} is the spindown luminosity of the magnetar, R is the radial distance of the nebula-ejecta boundary from the center of the magnetar, $t_{\text{diff}}^{\text{neb}}$ and $t_{\text{diff}}^{\text{ej}}$ are the photon diffusion timescales in the nebula and in the ejecta, respectively, \mathcal{A} is the fraction of non-thermal photons

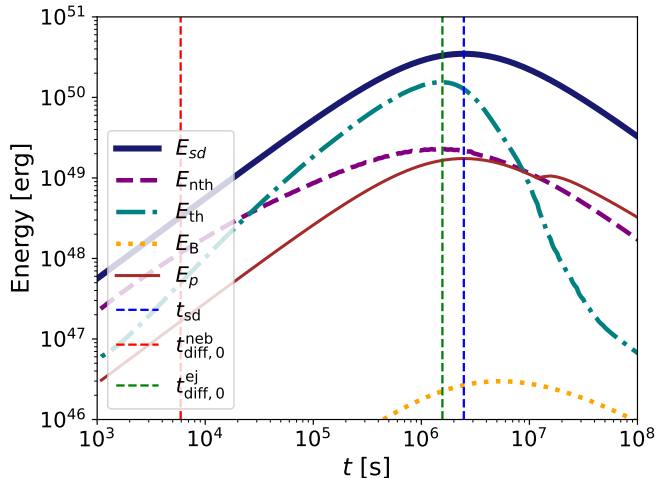


Figure 2. Time evolution of various components of the energy along with spin down and characteristic nebula and ejecta diffusion timescales, for our fiducial magnetar model for SN2017egm.

that escape from the ejecta, ε_B is a parameter that determines the magnetic field strength in the nebula, and $Q_{\text{heat}}^{\text{Ni}}$ is the rate of heating from the radioactive decay of ^{56}Ni , discussed in Appendix B.1.

For the ejecta mass M_{ej} , kinetic energy E_{kin} , and elemental composition we use model the *3p65Dx2* of L. Dessart et al. (2016, see Table B2 there and also previous work in L. Dessart et al. 2015). The initial velocity of the ejecta is given by $v_{\text{ej}} = \sqrt{2E_{\text{kin}}/M_{\text{ej}}}$. Given these ejecta properties, we scanned over the dipole field strength (B_d) and initial spin period P_i of the magnetar, finding that the combination $\{B_d = 5 \times 10^{13}$ G, $P_i = 4$ ms $\}$ results in an optical light curve most closely matching the $L_{\text{bol}}(t)$ and $T_{\text{th}}(t)$ evolution of SN 2017egm (Figure 1). The parameters of the progenitor star, ejecta, and magnetar remnant are summarized in Table 1.

Given these parameters, the evolution of the various energies, obtained from solving Equations (1), (2), and (3), are shown in Figure 2. The spindown energy peaks around the spindown timescale (t_{sd}), defined as the ratio between the initial rotational energy of the magnetar and the initial spindown luminosity $L_{\text{sd}}^{\text{init}}(P_i, B_d)$. For the fiducial parameter set, we have $t_{\text{sd}} \sim 2.5 \times 10^6$ s and the peak of $E_{\text{sd}} \sim 4 \times 10^{50}$ erg. The non-thermal energy, $E_{\text{nth}} \propto E_{\text{sd}}$ and hence closely follows the evolution of E_{sd} at initial times. However, as diffusion from the nebula starts becoming relevant after the characteristic timescale $t_{\text{diff},0}^{\text{neb}} \sim 5.9 \times 10^3$ s, non-thermal photons begin to diffuse out of the nebula through the ejecta, which leads to the evolution of E_{nth} to deviate from E_{sd} . The thermal energy evolution dominates the non-thermal component for $t \gtrsim 2 \times 10^4$ s.

This can be understood by the fact that the source term for the thermal photons is the reprocessed component of the non-thermal photons (Equation 2), where the fraction of reprocessed component is given by $(1 - \mathcal{A})$, \mathcal{A} being the ejecta albedo. This albedo is systematically evaluated based on the ejecta composition and its ionization state⁷. For $t \lesssim 10^6$ s, $\mathcal{A} \sim 0$ and hence most of the non-thermal photons are reprocessed into thermal photons. However, given the ejecta mass and composition, they are opaque to thermal photons for $t < t_{\text{diff},0}^{\text{ej}} \sim t_{\text{sd}}$, when most of the spindown energy is deposited, leading to E_{th} dominating over E_{nth} . At late times $t > t_{\text{diff},0}^{\text{ej}} \sim 1.6 \times 10^6$ s not only does E_{sd} decrease, but also diffusion of thermal photons becomes significant and hence E_{th} decreases rapidly.

The magnetic energy in the nebula $E_B \propto E_{\text{sd}}$ and therefore closely follows the injected spin-down energy E_{sd} in proportion to the nebula magnetization, ε_B . Although the magnetar wind on small scales is dominated by Poynting flux and extremely highly magnetized, various dissipation processes can occur in the wind and nebula that may act to reduce the magnetic field at the expense of plasma heating. Following model fits to optical light curve of 2017egm (M. Nicholl et al. 2017, 2018) by I. Vurm & B. D. Metzger (2021), we take $\varepsilon_B \sim 10^{-4}$. We discuss the energy placed into relativistic protons E_p in Section 3.2.

3.1. Electron and photon spectra

Here we discuss the pair injection spectra, the resulting photons, and their attenuations in our model. The magnetar wind is composed of pairs extracted from the magnetosphere as a result of $B - \gamma$ and $\gamma - \gamma$ processes. At initial times, the bulk Lorentz factor of the wind $\Gamma_w \gg 1$, that is, it is in the ultra-relativistic regime. However, its encounter with the expanding ejecta decelerates the wind, which leads to dissipation of their kinetic energy and formation of a wind termination shock (TS). The shocked region downstream of the TS forms the hot nebula, where the bulk kinetic energy of the wind is converted into particle energy and magnetic fields. Thus, the distribution of particles in the downstream will naturally be influenced by the upstream bulk wind Lorentz factor Γ_w , setting a characteristic energy scale. We can define Γ_w as

$$\Gamma_w \approx \frac{L_{\text{sd}}}{4\pi m_e c^2 n_{e\pm}^w R_s^2 c}, \quad (4)$$

⁷ We assume that the ejecta elements are singly ionized, which is a reasonable approximation given that the most abundant element in the ejecta, He, is largely neutral (N. Ekanger et al. 2026). The ionization state most prominently affects the free-free absorption and hence the late time radio emission.

Table 1. Model parameters

Stellar progenitor, supernova ejecta, and magnetar properties

M_i	M_f	M_*	R_*	I	M_{ej}	E_{kin}	P_i	B_d	v_{ej}	κ_{ej}
$16 M_\odot$	$3.65 M_\odot$	$1.42 M_\odot$	10^6 cm	10^{45} g cm^2	$2.23 M_\odot$	$5.08 \times 10^{51} \text{ erg}$	4 ms	$5 \times 10^{13} \text{ G}$	$0.05 c$	$0.1 \text{ cm}^2 \text{ g}^{-1}$

Elemental ejecta composition from Model *3p65Dx2* of L. Dessart et al. (2016)

Element	H	He	C	N	O	Si	S	Ca	Fe	Co	^{56}Ni
Comp. ($M_\odot \times 10^{-2}$)	0.464	155	9.33	1.07	25.1	7.64	2.86	0.548	0.360	0	10.5
Num Frac. (N_0)	0.0109	0.9184	0.0184	0.0018	0.0372	0.0064	0.0021	0.0003	0.0002	0.0	0.0042

where the rate of energy extraction by the wind $L_w \sim L_{\text{sd}}$, the pair number density in the wind region is given by $n_{e^\pm}^w$, R_s is the approximate radial distance of the TS from the central engine. We assume that the pairs entering the nebula at the TS are well-described by a broken power law injection set by the break Lorentz factor of the pairs $\gamma_{e,\text{br}} \approx \Gamma_w$. Hence, the primary pair injection spectrum has the following form

$$Q_e^{\text{inj}}(\gamma_e) = Q_e^0 \exp\left(-\frac{\gamma_e}{\gamma_{e,\text{cut}}}\right) \begin{cases} \left(\frac{\gamma_e}{\gamma_{e,\text{br}}}\right)^{-1.5}, & \gamma_m \leq \gamma_e \leq \gamma_{e,\text{br}} \\ \left(\frac{\gamma_e}{\gamma_{e,\text{br}}}\right)^{-2.5}, & \gamma_{e,\text{br}} < \gamma_e \leq \gamma_M, \end{cases} \quad (5)$$

where the electron Lorentz factor $\gamma_e = \varepsilon_e/(m_e c^2)$, ε_e is the comoving energy of the electron, γ_m and γ_M are the minimum and maximum electron Lorentz factors chosen to be 1 and 10^9 respectively (note that this choice has no consequence on the results). The cut-off Lorentz factor $\gamma_{e,\text{cut}}$ is determined self-consistently by balancing the cooling and acceleration timescales for the electrons. The normalization $Q_e^0 = L_{\text{sd}}^{\text{com}}/(m_e c^2 \int d\gamma_e \gamma_e Q_e^{\text{inj}}(\gamma_e)/Q_e^0)$, where $L_{\text{sd}}^{\text{com}}$ is the comoving L_{sd} . The pair multiplicity⁸ in the wind and the nebula can be defined as $Y = \dot{N}_{e^\pm}^c m_e c^2 / L_{\text{sd}}$, where $\dot{N}_{e^\pm}^c$ is the pair creation rate in the wind or nebular regions. This is important in determining the diffusion timescale of the photons in the nebula (see Equation 1) $t_{\text{diff}}^{\text{neb}} \approx (R/c)(1+\tau_{\text{diff}}^{\text{neb}})$, where the Thomson optical depth is given by $\tau_{\text{diff}}^{\text{neb}} \approx (4Y L_{\text{sd}} \sigma_T / (\pi m_e c^3 R \Gamma_{\text{ej}}^2))^{1/2}$. Appendices A.1 and A.2 provide a detailed calculation of the pair multiplicity and the bulk wind Lorentz factor, respectively.

⁸ Note that the pair multiplicity defined here by Y is analogous to the *pair yield*, that is, the fraction of injected power converted into pair rest mass, as described in R. Svensson (1987) (see Equation 2.25 there) and A. A. Zdziarski (1988) (see Equation 12 there).

The injected pairs are transported and the quasi-steady state spectrum is obtained by considering synchrotron, inverse Compton (IC), and dynamical losses. The energy distribution of the non-thermal photons are then computed through the full electromagnetic cascade via synchrotron, IC, and $\gamma\gamma$ processes. The energy density of the thermal photons can be evaluated using the thermal temperature $T_{\text{th}} \propto E_{\text{th}}^{1/4}$. IC scattering of thermal photons which have a large energy density dominates the non-thermal photon spectra, while synchrotron is significant for $E_\gamma \lesssim 1 \text{ eV}$. At low energies ($E_\gamma \lesssim 1 \text{ eV}$), synchrotron self-absorption (SSA) effects become important and at high energies ($E_\gamma \gtrsim 10 \text{ GeV}$) Klein-Nishina and $\gamma\gamma$ pair production suppress the energy density in non-thermal photons. The latter is also taken into account consistently in our model where we compute the secondary pairs produced from $\gamma\gamma$ pair production processes to account for the non-thermal photons. The resulting photon spectra in the nebula is discussed in Appendix B.2 and will be relevant for providing the radiation field for neutrino production discussed in Section 3.2.

The nebular photons further suffer attenuation in the supernova ejecta via free-free, bound-bound, bound-free, Compton, and Bethe-Heitler processes in the radio, IR/Optical/UV, UV/X-ray, MeV, GeV-TeV wavelengths. We present the relevant details about attenuation across various wavelengths and its evolution with time in Appendix B.3.

3.2. Neutrino production

In this subsection, we discuss the proton injection spectrum, acceleration of the injected CR protons, and their subsequent interactions resulting in neutrino production from magnetar-powered SLSNe. We consider neutrino production in the nebular and the ejecta regions. The former is dominated by photohadronic ($p\gamma$) interactions, while the latter by hadronuclear (pp) interactions owing to the dense ejecta.

The plasma within the magnetosphere of the pulsar is dragged along the magnetic field lines and hence co-rotates with the magnetar. This co-rotation of charged particles creates an electric field, a component of which is not perpendicular to the magnetic field. This electric field can be used to extract charges from the surface of the magnetar. For simplicity, we restrict ourselves to protons⁹. The maximum charge density that can be extracted can be estimated using the Goldreich-Julian charge density (P. Goldreich & W. H. Julian 1969) such that the rate of CR proton production is given by $\dot{N}_p = ((4\pi^2/ec)(R_*^3 B_d/P^2))$, where the spin period evolution is governed by $P(t) = P_i(1 + t/t_{sd})^{1/2}$.

The polar cap region of the magnetar is capable of accelerating protons in the potential gap. Thus, the injection spectra $d\dot{N}_p^{\text{inj}}/d\varepsilon'_p = \dot{N}_p \delta(\varepsilon'_p - \varepsilon'_p{}^{\text{cutoff,pc}})$, where $\varepsilon'_p{}^{\text{cutoff,pc}}$ is the cut-off energy in the polar cap region. The primed quantities denote the comoving quantities unless otherwise stated. The Dirac-delta function for the injection spectra (J. Arons 2003) is motivated by the fact that the potential gap created by the electric field is shorted at periodic intervals and therefore the CR protons are accelerated at discrete energies. The cut-off energy for the protons in the polar cap region (which determine their injection spectra) is obtained by comparing the maximum energy that the protons can gain while they are accelerated across the potential gap and the energy loss due to curvature radiation, such that at any instant the minimum energy of the two is chosen as $\varepsilon'_p{}^{\text{cutoff,pc}}$.

The CR protons can also be re-accelerated at the TS as a result of shocks or magnetic reconnection (L. Sironi & A. Spitkovsky 2011, 2014). The cutoff in the TS region $\varepsilon'_p{}^{\text{cutoff,TS}}$ is obtained by balancing the acceleration and cooling timescales for the protons. This finally gives the maximum energy to which the CR protons can be accelerated as $\varepsilon_p^{\text{max}} = \min[\varepsilon'_p{}^{\text{cutoff,pc}}, \varepsilon'_p{}^{\text{cutoff,TS}}]$. The evolution of $\varepsilon'_p{}^{\text{cutoff,pc}}$, $\varepsilon'_p{}^{\text{cutoff,TS}}$, and $\varepsilon_p^{\text{max}}$ is discussed in Appendix C.1. The total energy in protons which can be estimated using $E_p(t) = \dot{N}_{p,\text{inj}} \varepsilon_p^{\text{max}} t$ peaks around t_{sd} and is shown as a brown line in Figure 2.

The quasi-steady state energy spectrum for the accelerated CR protons in the nebula ($dN_p/d\varepsilon'_p$) is obtained by solving the transport equation (S. S. Kimura et al. 2019) taking into account cooling and escape. The CR protons then interact with the photons or protons in the nebula and ejecta to produce charged and neutral pions amongst other decay products. A fraction of the charged

pions produce neutrinos while the neutral pions produce photons. Since the nebula is filled with non-thermal and thermal photons, the CR protons mostly cool through the photomeson channel, while the ejecta consists of a large number of protons and hence pp interactions serve as the dominant cooling channel. The relevant acceleration and cooling timescales for the CR protons are discussed in Appendix C.2. To compute the neutrino spectra we use the fitting formulae from S. R. Kelner & F. A. Aharonian (2008). The suppression factors associated with the cooling of pions and muons are also taken into account consistently. For the observed neutrino spectra, we also account for the oscillation effects during their propagation from the SLSNe to an observer on Earth.

For the pp component in the ejecta, the comoving target nucleon number density can be estimated $n_p^{\text{ej}} = \rho^{\text{ej}}/m_u$, where ρ^{ej} is the comoving density of the ejecta and m_u is the atomic mass unit. The CR protons that escape the nebula serve as the source for the pp interactions in the ejecta, such that the injection rate is given by $d\dot{N}_p^{\text{inj,ej}}/d\varepsilon'_p = (dN_p/d\varepsilon'_p)/t'_{\text{esc}}$, $t'_{\text{esc}} = \max[R^2/D_c(\varepsilon'_p), R/c]$ is the escape timescale of CR protons in the nebula, the first term accounts for diffusion (D. Harari et al. 2014) while the second term accounts for free-streaming of the protons from the nebula to the ejecta. The pp interaction rate can be estimated as $t_{pp}^{-1,\text{ej}} \simeq n_p^{\text{ej}} \sigma_{pp} \kappa_{pp} c$, where σ_{pp} and κ_{pp} are the proton interaction cross-section and inelasticity respectively (S. R. Kelner et al. 2006). The quasi-steady state CR proton spectrum in the ejecta is given by $dN_p^{\text{ej}}/d\varepsilon'_p = (d\dot{N}_p^{\text{inj,ej}}/d\varepsilon'_p) t'_{\text{loss}}{}^{\text{ej}}$, where $t'_{\text{loss}}{}^{\text{ej}} = t_{pp}^{-1,\text{ej}} + t_{\text{exp}}^{-1,\text{ej}} + t_{\text{esc}}^{-1,\text{ej}}$. The expansion timescale of the ejecta is given by $t_{\text{exp}}^{\text{ej}} = R/(\Gamma_{\text{ej}} v)$ and $t_{\text{esc}}^{\text{ej}}$ represents the escape timescale of the protons from the ejecta. Similar to the neutrino computation in the nebula, the resulting ejecta proton spectrum $dN_p^{\text{ej}}/d\varepsilon'_p$ is then used to compute the secondary gamma rays, pairs, and neutrinos. We further include synchrotron cooling of secondary pions and muons before applying flavor mixing to obtain the total all-flavor neutrino output from the ejecta.

4. OBSERVATIONAL SIGNATURES

This section focuses on the main results of this work, that is, the observational multi-wavelength EM and neutrino signatures from a canonical magnetar-powered SLSNe, like SN 2017egm, at a typical source distance $d_L = 100$ Mpc. We present our results in the context of current and upcoming EM and neutrino telescopes and elaborate on their detection prospects.

⁹ For a discussion on ions or nuclei see discussion in M. Mukhopadhyay et al. (2025).

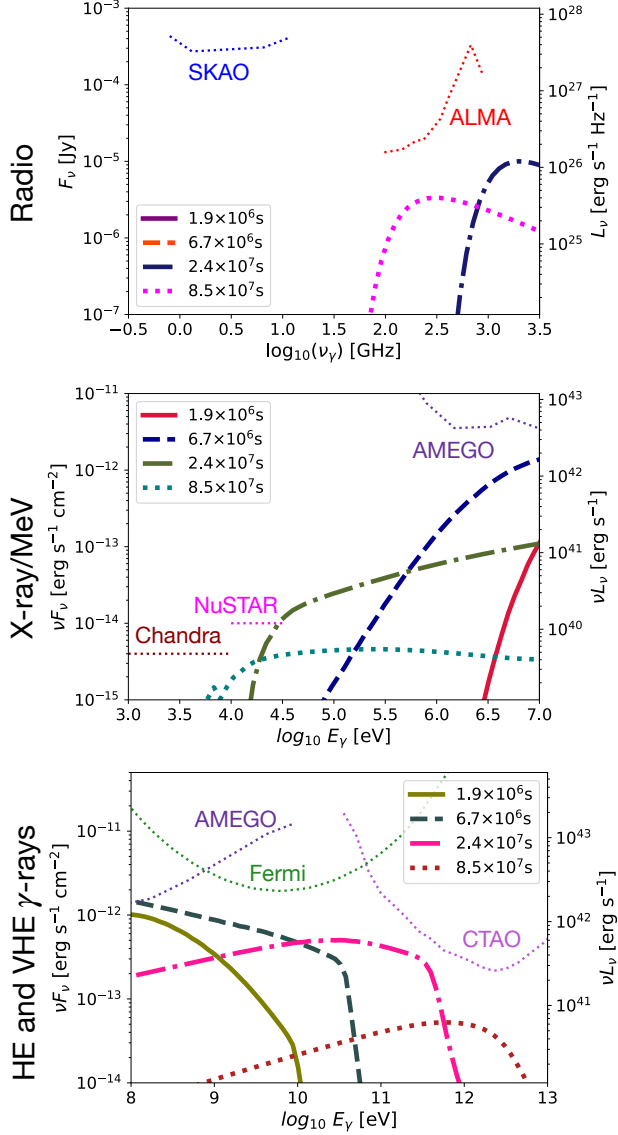


Figure 3. Predicted electromagnetic spectra from our fiducial magnetar-powered SLSNe model at 100 Mpc corresponding to the radio, X-ray, MeV, and gamma-ray bands at different time snapshots. The sensitivity curves for the relevant detectors in the given EM bands are also shown. Note that F_ν denotes spectral flux density, L_ν is the spectral luminosity, and νL_ν is the differential luminosity. The radio spectra (*top*) shows flux density while the *middle* and *bottom* panels show flux.

4.1. Electromagnetic signatures

We divide the observational EM signatures into different wavelengths and discuss their corresponding features and detectability given the relevant telescopes in that band. The predicted photon spectra in the mm/radio, X-ray/MeV, and GeV and TeV bands for different temporal snapshots are shown in Figure 3. Sensitivity curves for various current and upcoming obser-

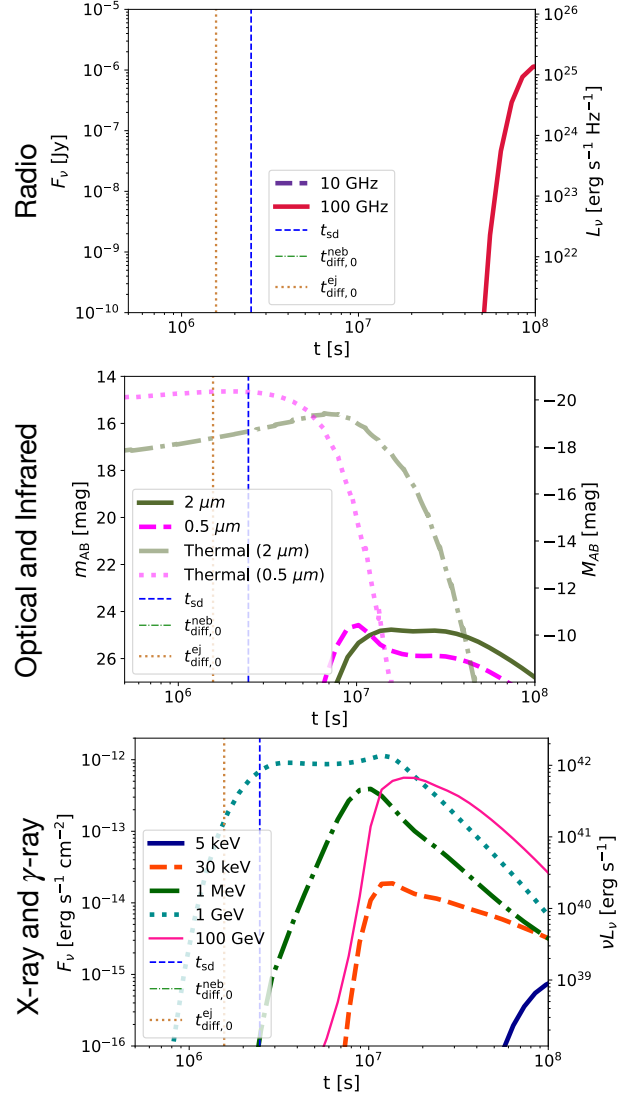


Figure 4. Light curves from a SLSNe at 100 Mpc corresponding to the radio, optical, infrared, X-ray and gamma-ray bands. The characteristic spindown (t_{sd}) and ejecta diffusion ($t_{diff,0}^{ej}$) timescales are also shown. The representative frequencies (for radio), wavelengths (for optical and infrared), and energies (for X-ray and γ -rays) are motivated by relevant bands from observational telescopes shown in Figure 3. The apparent and absolute magnitudes are shown by m_{AB} and M_{AB} respectively.

vational facilities (see Table 1 in [M. Mukhopadhyay & S. S. Kimura 2025](#), acronyms, and references therein) are also overlaid. Sources of photon attenuation relevant for interpreting features in the EM spectra are discussed in Appendix B.3. Light curves are shown in Figure 4 and correspond to radio, optical, infrared, X-ray, and gamma-ray bands. For comparison, we overlay the spindown and other key timescales as vertical lines.

The radio band spectrum is cut-off at low frequencies by SSA in the nebula and free-free absorption in the ejecta, respectively, both of which decrease monotonically in frequency with time as the system expands. Even at late times (\sim a few years post-collapse) free-free absorption in the ejecta completely attenuates $\lesssim 100$ GHz emission. Millimeter/sub-mm radio telescopes like ALMA can potentially detect the late time radio emission as can be inferred from the 100 GHz radio light curve. However, at these frequencies the forward shock (afterglow) generated as the ejecta collides with circumstellar material might outshine our predicted signal (M. Chen et al. 2026). Moreover, the radio signal might also be enhanced at late times from pairs that accumulate in the nebula over time (e.g., B. Margalit & B. D. Metzger 2018), which our current model does not take into account.

The ejecta attenuation, which depends on its elemental composition, also suppresses the observed X-ray and MeV photon spectra. The observation of soft X-rays in telescopes like Chandra or XMM-Newton are thus unlikely, which can also be noted from the 5 keV X-ray light curve having a tiny ($\sim 10^{-15}$ erg s $^{-1}$ cm $^{-2}$) flux at very late times. However, hard X-rays are likely to be observed providing NuSTAR with optimistic detection prospects. For a typical NuSTAR detection band of 30 keV, the light curve reaches a peak sensitivity of \sim a few 10^{-14} erg s $^{-1}$ cm $^{-2}$ at ~ 1 year post collapse. In the MeV band, the peak occurs $\sim 10^7$ s post collapse corresponding to the ejecta becoming transparent to MeV wavelengths. This indicates that upcoming telescopes like AMEGO/AMEGO-X can potentially detect the source.

The dominant source of attenuation of GeV gamma-rays are by $\gamma\gamma$ pair production in the nebula, Bethe-Heitler, and Compton processes in the ejecta. However, the $\gamma\gamma$ cutoff energy shifts to higher energies with time, allowing for \sim TeV emission within a year from collapse; the ejecta becomes completely transparent to gamma-rays on a similar timescale. The situation is even better for GeV gamma rays which can become observable in telescopes like Fermi roughly around spindown timescale. Since the GeV photons are effectively unattenuated around t_{sd} , the GeV lightcurve peaks around $t \sim t_{\text{sd}}$ and subsequently forms a plateau. Thus, GeV gamma ray telescopes like Fermi indeed have optimistic chances of detecting high-energy gamma-ray emission from magnetar-powered SLSNe. Thus, the observed evidence of GeV emission from SN 2017egm and the compatibility of our predictions for GeV gamma-rays is not surprising (see Figure 1 *bottom* panel). Moreover, at later stages very high-energy gamma-rays in the 100

GeV band might also be detected by CTAO from such a source.

The *middle* panel of Figure 4 shows both the thermal and non-thermal optical light curves. As discussed in Section 3, the thermal components completely dominate over the non-thermal component for SLSNe¹⁰. We note that as expected, with a peak absolute AB magnitude of ~ -20 , SLSNe are optically very bright. Thus, optical telescopes like Rubin LSST, will be observing $\mathcal{O}(10^5)$ SLSNe within the next decade (see Appendix D), assuming Rubin LSST observes 1/3 of all SLSNe. The SLSNe catalogs obtained from these surveys will then allow for stacking searches for detecting neutrino counterparts and gaining further insights into the properties of SLSNe.

4.2. Neutrino signatures

The observed all-flavor neutrino fluence resulting from our canonical magnetar-powered SLSNe, including both the $p\gamma$ component in the nebula and the pp component in the ejecta, is shown in Figure 5 (*left*). Relevant results for maximum proton energy and timescales are shown in Appendices C.1 and C.2, respectively. To illustrate the temporal evolution of the resulting neutrino fluence, we compute the fluence integrated over successive logarithmic time bins spanning half a decade. Furthermore, for comparison we show the point source sensitivities of upcoming neutrino telescopes like IceCube-Gen2 (M. G. Aartsen et al. 2021; IceCube-Gen2 Collaboration 2024) and Giant Radio Array for Neutrino Detection (GRAND-200k, J. Álvarez-Muñiz et al. 2020).

The neutrino fluence peaks in the energy range $10^7 - 10^8$ GeV at a fluence $\sim 3 \times 10^{-3}$ GeVcm $^{-2}$ on a timescale of a few weeks to a month, $t \sim 10^6 - 10^{6.5}$ s post collapse. This is reasonable because the total energy in protons peaks near the spindown timescale around $E_p \sim 1.7 \times 10^{49}$ erg (from Figure 2). Thus, the peak neutrino fluence can be estimated using $E_\nu^2 J_\nu \sim (1/(4\pi d_L^2))(3/8)E_p f_{p\gamma} f_{\text{bol}} f_{\pi, \text{sup}}$, where $f_{p\gamma}$, f_{bol} , and $f_{\pi, \text{sup}}$ are the $p\gamma$ efficiency, bolometric correction factor, and the pion suppression factors respectively. For the relevant timescales $f_{p\gamma} \approx f_{\text{bol}} \approx f_{\pi, \text{sup}} \approx 1$, giving $E_\nu^2 J_\nu \sim 0.003$ GeVcm $^{-2}$. The pp component in the ejecta also peaks in the energy range $10^7 - 10^8$ GeV but at a fluence $\sim 3 \times 10^{-4}$ GeVcm $^{-2}$, an order of magnitude lower than the $p\gamma$ component in the nebula. However at late times, $t \gtrsim 10^{6.5}$ s the pp component dominates the neutrino fluence for $E_\nu \gtrsim 10^8$ GeV while for $t \gtrsim 10^7$

¹⁰ Although completely overwhelmed by the thermal emission at optical wavelengths, the non-thermal component is constrained by hard X-ray and gamma-ray observations.

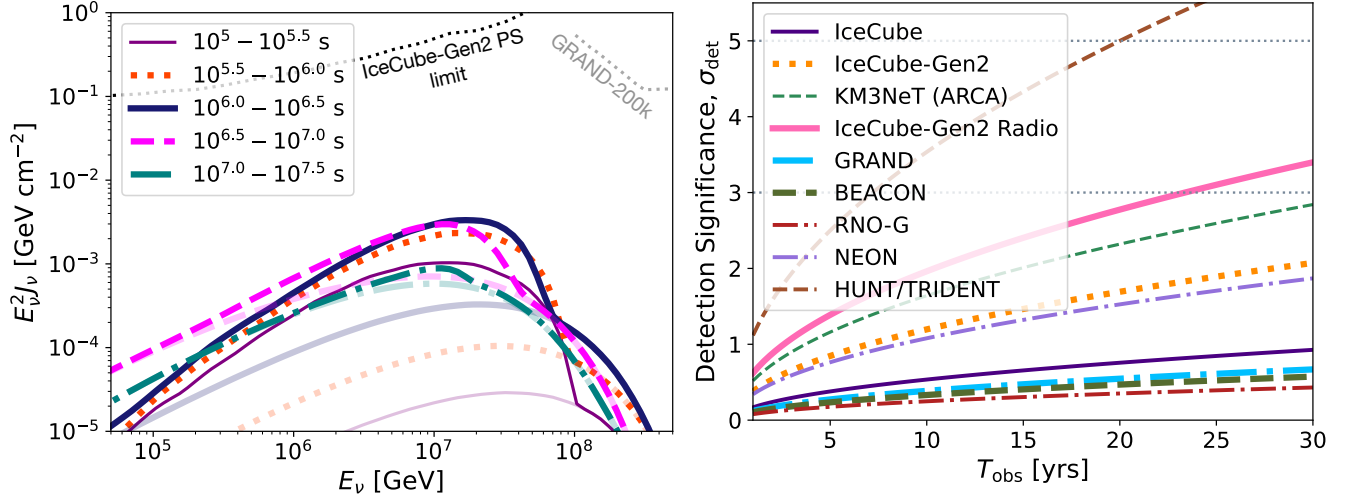


Figure 5. *Left:* Observed neutrino fluence (all-flavors) for a magnetar-powered SLSN at 100 Mpc for timescales post core-collapse ranging from a few hours to a year. The corresponding pp component from the ejecta is shown in fainter shades. *Right:* The detection significance for various current, upcoming, and proposed neutrino telescopes given the observation time (T_{obs}) as a result of stacking a population of observed SLSNe using Rubin LSST within redshift of $z_{\text{max}} = 1$, where we assume Rubin LSST observes 1/3 of all SLSNe. Note that the all-flavor day-averaged effective area including the appropriate field of view is used (see Appendix D for details) for IceCube, RNO-G, IceCube-Gen2, IceCube-Gen2 Radio, GRAND, and BEACON.

s, the pp component dominates over the $p\gamma$ component across almost the entire energy range.

For a single source, that is, a canonical SLSNe at 100 Mpc, the detection prospects with upcoming neutrino telescopes like IceCube-Gen2 or GRAND-200k appear dim. However, this problem can be mitigated by combining data from EM observations to perform the neutrino searches. The current era of powerful EM telescopes like Rubin LSST is ideal for searches of optical transients, like SLSNe. This allows for construction of data catalogs in various individual or a combination of EM wavelengths. These catalogs can then be used to perform maximum log-likelihood searches, where the likelihood functions are designed based on spatial, temporal, and energy correlations between the neutrino and the EM datasets, effectively *stacking* neutrino observations across multiple sources (see for example M. Mukhopadhyay et al. 2024a,b, 2026).

A simple estimate of the results for stacking of neutrino observations using a population of observed SLSNe in Rubin LSST within redshift $z_{\text{max}} = 1$ is presented in the *right* panel of Figure 5. We show the detection significance σ_{det} , for a given neutrino telescope as a function of the observation duration T_{obs} , where we assume given the field of view of Rubin LSST, it can observe a fraction 1/3 of all SLSNe at $z_{\text{max}} \leq 1$. Details regarding the computation of σ_{det} are provided in Appendix D. We note that the proposed $\sim 10 \text{ km}^3$ neutrino telescopes like HUNT or TRIDENT can reach 3σ (5σ) detection significance in less than 5 (20) years, while upcoming neutrino detectors like IceCube-Gen2 with the optical and radio

arrays can detect several signal neutrino events from a population of SLSNe within 10 years of observation and reach 3σ detection significance in ~ 20 years independently. Since the observed neutrino fluence peaks between $10^7 - 10^8$ GeV, detectors like IceCube-Gen2 and HUNT/TRIDENT with an effective area maximized across the relevant energies provides the best observational scenario.

It is also important to carefully choose the maximum redshift of the population one should consider for stacking searches. The number of SLSNe obviously increases with z , but beyond a critical redshift $z_{\text{max}} \sim 1$ the additional signal from more distant sources is not sufficient to overcome the background. To avoid a resulting reduction in the detection significance, this necessitates that optical observations of SLSNe also include redshift information from spectroscopic observations or photometric host galaxy information to filter the sample used in stacking analysis for neutrinos. Rubin LSST will provide photometric data which would need to be complemented by current generation telescopes like Subaru (N. Tamura et al. 2016), Gemini, Keck or next-generation ones like European Extremely Large Telescope (E-ELT) (C. Evans et al. 2015), US Extremely Large Telescope (US-ELT) (M. L. Graham et al. 2019; D. Milisavljevic et al. 2019) comprising of Thirty Meter Telescope (TMT) and the Giant Magellan Telescope (GMT) to obtain the spectroscopic observations.

5. CONCLUSIONS AND OUTLOOK

We address two main themes in this work – (a) a prediction for the the multi-wavelength EM and neutrino signatures from a canonical magnetar-powered SLSN and (b) highlighting the complementarity of the EM observations given their excellent detection prospects across wavelengths (particularly optical/IR band at Rubin and Roman) to search for neutrino signatures from a population of SLSNe.

Among the possible energy sources behind SLSNe is a millisecond magnetar, that is a remnant neutron star with a millisecond spin period and strong dipole magnetic field $10^{13} - 10^{15}$ G. We modeled our system by considering observational data from the nearest observed SLSNe SN 2017egm, in particular the bolometric luminosity and thermal temperature (see Figure 1). The properties of the ejecta, including mass and composition, were chosen based on numerical simulations of ejecta resulting from core-collapse. Remarkably, our model’s predictions for high-energy (GeV) gamma-rays are consistent with recent observational data from Fermi LAT (see Figure 1 *lower panel*), strengthening the conclusions of S. Li et al. (2024).

The magnetar’s rotational energy serves as the main reservoir for powering all thermal, non-thermal, and neutrino emissions (see Figure 2). This is achieved by systematically solving for the dynamics of the magnetar-wind-nebula-ejecta system and then computing the resulting leptonic and hadronic cascades and interactions. In particular, we also improve several aspects of our model at the microphysics level. Instead of arbitrarily fixing the break of the pair injection spectra, we consistently evaluate the bulk Lorentz factor of the wind to inject the non-thermal pairs accordingly. Furthermore, we also compute the pair multiplicity in the wind and nebula region rather than choosing a fixed value. These results are highlighted in Appendices A.1 and A.2 and provide more realistic observational signatures.

Even with the improvements to our model included here, it still makes several simplifying approximations. Firstly our model computes the lepto-hadronic interactions in an one-zone approximation. A more detailed computation can be performed by considering multi-zone emission models, where the photosphere evolves with time, which can be achieved by considering a spatially varying density profile ($\rho_{\text{ej}} \propto r^{-\delta}$) and thermal energy density ($\varepsilon_{\text{th}} \propto r^{-\Gamma}$) associated with the ejecta. This would presumably enable a better fit to the photosphere temperature T_{th} at the cost of introducing additional parameters for the ejecta density structure. The ionization state of the ejecta is another uncertainty as-

sociated with our modeling. For simplicity we consider singly-ionized ejecta, but recombination of the ejecta as it expands and cools could lead to more optimistic radio signatures. Radio signatures can also be boosted as a result of emission from older pairs in the nebula (B. Margalit & B. D. Metzger 2018) or from shock breakout (M. Chen et al. 2026). We leave these for future work.

We present the results of theme (a) in Figures 3 and 4 for the EM signatures and Figure 5 (*left panel*) for the neutrino signatures. The results corresponding to theme (b) are shown in the *right panel* of Figure 5. We show that stacking searches using a population of SLSNe collected from future EM surveys such as LSST, enable proposed and upcoming neutrino telescopes to detect several signal events over a timescale of ~ 10 years; in particular, HUNT/TRIDENT can reach 3σ and 5σ detection significance in less than 5 and 20 years respectively. IceCube-Gen2 Radio and GRAND can also independently reach 3σ detection significance in roughly 2 decades of observation time. The detection of neutrinos from a population of SLSNe will take us a step forward in understanding the dynamics and most importantly in unraveling the energy source for SLSNe in the very near future. The current work brings forth the possibilities to gain deeper insights into the engines of SLSNe, enabled by the joint progress in optical transient and neutrino astronomy.

ACKNOWLEDGEMENTS

We thank Kazumi Kashiyama for useful discussions. M.M acknowledges support from the Fermi-Forward Discovery Group, LLC under Contract No. 89243024CSC000002 with the U.S. Department of Energy, Office of Science, Office of High Energy Physics. S.S.K acknowledges the support by KAKENHI No. 22K14028, No. 21H04487, No. 23H04899, and the Tohoku Initiative for Fostering Global Researchers for Interdisciplinary Sciences (TI-FRIS) of MEXT’s Strategic Professional Development Program for Young Researchers. B.D.M acknowledges support from the National Science Foundation (grant AST-2406637), NASA (grant 80NSSC26K0299), and the Simons Foundation (grant 727700). The Flatiron Institute is supported by the Simons Foundation. I.V acknowledges support by the Estonian Research Council (grant PRG2159), Estonian Ministry of Education and Research (grant TK202), and the European Union’s Horizon Europe research and innovation programme (EXCOSM, grant No. 101159513).

REFERENCES

- Aartsen, M. G., et al. 2021, *J. Phys. G*, 48, 060501, doi: [10.1088/1361-6471/abbd48](https://doi.org/10.1088/1361-6471/abbd48)
- Abbasi, R., et al. 2021, *Phys. Rev. D*, 104, 022002, doi: [10.1103/PhysRevD.104.022002](https://doi.org/10.1103/PhysRevD.104.022002)
- Abbasi, R., et al. 2023, *Astrophys. J. Lett.*, 949, L12, doi: [10.3847/2041-8213/acd2c9](https://doi.org/10.3847/2041-8213/acd2c9)
- Abbasi, R., et al. 2024, *Phys. Rev. D*, 110, 022001, doi: [10.1103/PhysRevD.110.022001](https://doi.org/10.1103/PhysRevD.110.022001)
- Adrian-Martinez, S., et al. 2016, *J. Phys. G*, 43, 084001, doi: [10.1088/0954-3899/43/8/084001](https://doi.org/10.1088/0954-3899/43/8/084001)
- Álvarez-Muñiz, J., et al. 2020, *Sci. China Phys. Mech. Astron.*, 63, 219501, doi: [10.1007/s11433-018-9385-7](https://doi.org/10.1007/s11433-018-9385-7)
- Arons, J. 2003, *Astrophys. J.*, 589, 871, doi: [10.1086/374776](https://doi.org/10.1086/374776)
- Blum, B., et al. 2022, in *Snowmass 2021*.
<https://arxiv.org/abs/2203.07220>
- Bose, S., et al. 2018, *Astrophys. J.*, 853, 57, doi: [10.3847/1538-4357/aaa298](https://doi.org/10.3847/1538-4357/aaa298)
- Burrows, D. N., et al. 2005, *Space Sci. Rev.*, 120, 165, doi: [10.1007/s11214-005-5097-2](https://doi.org/10.1007/s11214-005-5097-2)
- Chen, M. 2026, *Nucl. Instrum. Meth. A*, 1086, 171374, doi: [10.1016/j.nima.2026.171374](https://doi.org/10.1016/j.nima.2026.171374)
- Chen, M., Kashiyama, K., & Sato, M. 2026, <https://arxiv.org/abs/2601.09552>
- Chen, Z. H., Yan, L., Kangas, T., et al. 2023, *ApJ*, 943, 41, doi: [10.3847/1538-4357/aca161](https://doi.org/10.3847/1538-4357/aca161)
- Chevalier, R. A., & Irwin, C. M. 2011, *ApJL*, 729, L6, doi: [10.1088/2041-8205/729/1/L6](https://doi.org/10.1088/2041-8205/729/1/L6)
- Delgado, A., Harrison, D., Hodgkin, S., et al. 2017, *Transient Name Server Discovery Report*, 2017-591, 1
- Dessart, L., Hillier, D. J., Waldman, R., Livne, E., & Blondin, S. 2012, *Mon. Not. Roy. Astron. Soc.*, 426, L76, doi: [10.1111/j.1745-3933.2012.01329.x](https://doi.org/10.1111/j.1745-3933.2012.01329.x)
- Dessart, L., Hillier, D. J., Woosley, S., et al. 2015, *Mon. Not. Roy. Astron. Soc.*, 453, 2189, doi: [10.1093/mnras/stv1747](https://doi.org/10.1093/mnras/stv1747)
- Dessart, L., Hillier, D. J., Woosley, S., et al. 2016, *Mon. Not. Roy. Astron. Soc.*, 458, 1618, doi: [10.1093/mnras/stw418](https://doi.org/10.1093/mnras/stw418)
- Eftekhari, T., et al. 2021, *Astrophys. J.*, 912, 21, doi: [10.3847/1538-4357/abe9b8](https://doi.org/10.3847/1538-4357/abe9b8)
- Ekanger, N., Kimura, S. S., & Kashiyama, K. 2026, <https://arxiv.org/abs/2602.06410>
- Enberg, R., Reno, M. H., & Sarcevic, I. 2008, *Phys. Rev. D*, 78, 043005, doi: [10.1103/PhysRevD.78.043005](https://doi.org/10.1103/PhysRevD.78.043005)
- Evans, C., Puech, M., Afonso, J., et al. 2015, *arXiv preprint arXiv:1501.04726*
- Fang, K., & Metzger, B. D. 2017, *ApJ*, 849, 153, doi: [10.3847/1538-4357/aa8b6a](https://doi.org/10.3847/1538-4357/aa8b6a)
- Fang, K., Metzger, B. D., Murase, K., Bartos, I., & Kotera, K. 2019, *ApJ*, 878, 34, doi: [10.3847/1538-4357/ab1b72](https://doi.org/10.3847/1538-4357/ab1b72)
- Gal-Yam, A. 2019, *Ann. Rev. Astron. Astrophys.*, 57, 305, doi: [10.1146/annurev-astro-081817-051819](https://doi.org/10.1146/annurev-astro-081817-051819)
- Gal-Yam, A., & Leonard, D. C. 2009, *Nat*, 458, 865, doi: [10.1038/nature07934](https://doi.org/10.1038/nature07934)
- Gal-Yam, A., Mazzali, P., Ofek, E. O., et al. 2009, *Nat*, 462, 624, doi: [10.1038/nature08579](https://doi.org/10.1038/nature08579)
- Goldreich, P., & Julian, W. H. 1969, *Astrophys. J.*, 157, 869, doi: [10.1086/150119](https://doi.org/10.1086/150119)
- Gomez, S., Nicholl, M., Berger, E., et al. 2024, *MNRAS*, 535, 471, doi: [10.1093/mnras/stae2270](https://doi.org/10.1093/mnras/stae2270)
- Graham, M. L., et al. 2019, <https://arxiv.org/abs/1904.05957>
- Harari, D., Mollerach, S., & Roulet, E. 2014, *Phys. Rev. D*, 89, 123001, doi: [10.1103/PhysRevD.89.123001](https://doi.org/10.1103/PhysRevD.89.123001)
- Honda, M., Kajita, T., Kasahara, K., Midorikawa, S., & Sanuki, T. 2007, *Phys. Rev. D*, 75, 043006, doi: [10.1103/PhysRevD.75.043006](https://doi.org/10.1103/PhysRevD.75.043006)
- IceCube-Gen2 Collaboration. 2024, *IceCube-Gen2 Technical Design Report*, Tech. rep. <https://icecube-gen2.wisc.edu/science/publications/tdr/>
- Ivezić, Ž., et al. 2019, *Astrophys. J.*, 873, 111, doi: [10.3847/1538-4357/ab042c](https://doi.org/10.3847/1538-4357/ab042c)
- Kasen, D., & Bildsten, L. 2010, *Astrophys. J.*, 717, 245, doi: [10.1088/0004-637X/717/1/245](https://doi.org/10.1088/0004-637X/717/1/245)
- Katz, B., Sapir, N., & Waxman, E. 2012, *Astrophys. J.*, 747, 147, doi: [10.1088/0004-637X/747/2/147](https://doi.org/10.1088/0004-637X/747/2/147)
- Kelner, S. R., & Aharonian, F. A. 2008, *Phys. Rev. D*, 78, 034013, doi: [10.1103/PhysRevD.78.034013](https://doi.org/10.1103/PhysRevD.78.034013)
- Kelner, S. R., Aharonian, F. A., & Bugayov, V. V. 2006, *Phys. Rev. D*, 74, 034018, doi: [10.1103/PhysRevD.74.034018](https://doi.org/10.1103/PhysRevD.74.034018)
- Kheirandish, A., & Murase, K. 2023, *Astrophys. J. Lett.*, 956, L8, doi: [10.3847/2041-8213/acf84f](https://doi.org/10.3847/2041-8213/acf84f)
- Kimura, S. S., Murase, K., & Mészáros, P. 2019, *Phys. Rev. D*, 100, 083014, doi: [10.1103/PhysRevD.100.083014](https://doi.org/10.1103/PhysRevD.100.083014)
- Kotera, K., Mukhopadhyay, M., Alves Batista, R., et al. 2026, *JCAP*, 01, 027, doi: [10.1088/1475-7516/2026/01/027](https://doi.org/10.1088/1475-7516/2026/01/027)
- Kotera, K., Phinney, E. S., & Olinto, A. V. 2013, *Mon. Not. Roy. Astron. Soc.*, 432, 3228, doi: [10.1093/mnras/stt680](https://doi.org/10.1093/mnras/stt680)
- Li, S., Liang, Y.-F., Liao, N.-H., Lei, L., & Fan, Y.-Z. 2024, <https://arxiv.org/abs/2407.05968>
- Margalit, B., & Metzger, B. D. 2018, *ApJL*, 868, L4, doi: [10.3847/2041-8213/aaedad](https://doi.org/10.3847/2041-8213/aaedad)
- Margalit, B., Metzger, B. D., Berger, E., et al. 2018, *Mon. Not. Roy. Astron. Soc.*, 481, 2407, doi: [10.1093/mnras/sty2417](https://doi.org/10.1093/mnras/sty2417)

- Metzger, B. D., Berger, E., & Margalit, B. 2017, *Astrophys. J.*, 841, 14, doi: [10.3847/1538-4357/aa633d](https://doi.org/10.3847/1538-4357/aa633d)
- Metzger, B. D., & Piro, A. L. 2014, *MNRAS*, 439, 3916, doi: [10.1093/mnras/stu247](https://doi.org/10.1093/mnras/stu247)
- Metzger, B. D., Vurm, I., Hascoet, R., & Beloborodov, A. M. 2014, *Mon. Not. Roy. Astron. Soc.*, 437, 703, doi: [10.1093/mnras/stt1922](https://doi.org/10.1093/mnras/stt1922)
- Milisavljevic, D., et al. 2019, <https://arxiv.org/abs/1904.05897>
- Moriya, T. J. 2024, <https://arxiv.org/abs/2407.12302>
- Mukhopadhyay, M., & Kimura, S. S. 2025, *Astrophys. J. Lett.*, 989, L41, doi: [10.3847/2041-8213/adf285](https://doi.org/10.3847/2041-8213/adf285)
- Mukhopadhyay, M., & Kimura, S. S. 2026, <https://arxiv.org/abs/2601.22266>
- Mukhopadhyay, M., Kimura, S. S., & Metzger, B. D. 2025, *Astrophys. J.*, 987, 2, doi: [10.3847/1538-4357/adc913](https://doi.org/10.3847/1538-4357/adc913)
- Mukhopadhyay, M., Kimura, S. S., & Murase, K. 2024a, *Phys. Rev. D*, 109, 043053, doi: [10.1103/PhysRevD.109.043053](https://doi.org/10.1103/PhysRevD.109.043053)
- Mukhopadhyay, M., Kotera, K., Wissel, S., Murase, K., & Kimura, S. S. 2024b, *Phys. Rev. D*, 110, 063004, doi: [10.1103/PhysRevD.110.063004](https://doi.org/10.1103/PhysRevD.110.063004)
- Mukhopadhyay, M., Wusinich, P., & Murase, K. 2026, <https://arxiv.org/abs/2601.20934>
- Murase, K. 2024, *Phys. Rev. D*, 109, 103020, doi: [10.1103/PhysRevD.109.103020](https://doi.org/10.1103/PhysRevD.109.103020)
- Murase, K., Kashiyama, K., Kiuchi, K., & Bartos, I. 2015, *Astrophys. J.*, 805, 82, doi: [10.1088/0004-637X/805/1/82](https://doi.org/10.1088/0004-637X/805/1/82)
- Murase, K., Kashiyama, K., & Mészáros, P. 2016, *Mon. Not. Roy. Astron. Soc.*, 461, 1498, doi: [10.1093/mnras/stw1328](https://doi.org/10.1093/mnras/stw1328)
- Murase, K., Thompson, T. A., Lacki, B. C., & Beacom, J. F. 2011, *Phys. Rev. D*, 84, 043003, doi: [10.1103/PhysRevD.84.043003](https://doi.org/10.1103/PhysRevD.84.043003)
- Murase, K., Thompson, T. A., & Ofek, E. O. 2014, *Mon. Not. Roy. Astron. Soc.*, 440, 2528, doi: [10.1093/mnras/stu384](https://doi.org/10.1093/mnras/stu384)
- Murase, K., et al. 2021, *Mon. Not. Roy. Astron. Soc.*, 508, 44, doi: [10.1093/mnras/stab2506](https://doi.org/10.1093/mnras/stab2506)
- Nicholl, M., Berger, E., Margutti, R., et al. 2017, *Astrophys. J. Lett.*, 845, L8, doi: [10.3847/2041-8213/aa82b1](https://doi.org/10.3847/2041-8213/aa82b1)
- Nicholl, M., et al. 2018, *Astrophys. J. Lett.*, 866, L24, doi: [10.3847/2041-8213/aae70d](https://doi.org/10.3847/2041-8213/aae70d)
- Ofek, E. O., et al. 2007, *Astrophys. J. Lett.*, 659, L13, doi: [10.1086/516749](https://doi.org/10.1086/516749)
- Omand, C. M. B., & Sarin, N. 2023, *Mon. Not. Roy. Astron. Soc.*, 527, 6455, doi: [10.1093/mnras/stad3645](https://doi.org/10.1093/mnras/stad3645)
- Pitik, T., Tamborra, I., Lincetto, M., & Franckowiak, A. 2023, *Mon. Not. Roy. Astron. Soc.*, 524, 3366, doi: [10.1093/mnras/stad2025](https://doi.org/10.1093/mnras/stad2025)
- Quimby, R. M., Aldering, G., Wheeler, J. C., et al. 2007, *Astrophys. J. Lett.*, 668, L99, doi: [10.1086/522862](https://doi.org/10.1086/522862)
- Quimby, R. M., et al. 2011, *Nature*, 474, 487, doi: [10.1038/nature10095](https://doi.org/10.1038/nature10095)
- Renault-Tinacci, N., Kotera, K., Neronov, A., & Ando, S. 2018, *Astron. Astrophys.*, 611, A45, doi: [10.1051/0004-6361/201730741](https://doi.org/10.1051/0004-6361/201730741)
- Sironi, L., & Spitkovsky, A. 2011, *Astrophys. J.*, 741, 39, doi: [10.1088/0004-637X/741/1/39](https://doi.org/10.1088/0004-637X/741/1/39)
- Sironi, L., & Spitkovsky, A. 2014, *Astrophys. J. Lett.*, 783, L21, doi: [10.1088/2041-8205/783/1/L21](https://doi.org/10.1088/2041-8205/783/1/L21)
- Smith, N., Chornock, R., Silverman, J. M., Filippenko, A. V., & Foley, R. J. 2010, *Astrophys. J.*, 709, 856, doi: [10.1088/0004-637X/709/2/856](https://doi.org/10.1088/0004-637X/709/2/856)
- Suzuki, A., & Maeda, K. 2017, *Mon. Not. Roy. Astron. Soc.*, 466, 2633, doi: [10.1093/mnras/stw3259](https://doi.org/10.1093/mnras/stw3259)
- Svensson, R. 1987, *MNRAS*, 227, 403, doi: [10.1093/mnras/227.2.403](https://doi.org/10.1093/mnras/227.2.403)
- Tamura, N., et al. 2016, *Proc. SPIE Int. Soc. Opt. Eng.*, 9908, 99081M, doi: [10.1117/12.2232103](https://doi.org/10.1117/12.2232103)
- Vurm, I., & Metzger, B. D. 2021, *Astrophys. J.*, 917, 77, doi: [10.3847/1538-4357/ac0826](https://doi.org/10.3847/1538-4357/ac0826)
- Woosley, S. E. 2010, *Astrophys. J. Lett.*, 719, L204, doi: [10.1088/2041-8205/719/2/L204](https://doi.org/10.1088/2041-8205/719/2/L204)
- Ye, Z. P., et al. 2023, *Nature Astron.*, 7, 1497, doi: [10.1038/s41550-023-02087-6](https://doi.org/10.1038/s41550-023-02087-6)
- Zdziarski, A. A. 1988, *ApJ*, 335, 786, doi: [10.1086/166967](https://doi.org/10.1086/166967)
- Zhang, H., Cui, Y., Huang, Y., et al. 2025, *Astropart. Phys.*, 171, 103123, doi: [10.1016/j.astropartphys.2025.103123](https://doi.org/10.1016/j.astropartphys.2025.103123)
- Zhu, J., et al. 2023, *Astrophys. J.*, 949, 23, doi: [10.3847/1538-4357/acc2c3](https://doi.org/10.3847/1538-4357/acc2c3)
- Zhu, J.-P., Liu, L.-D., Yu, Y.-W., et al. 2024, *Astrophys. J. Lett.*, 970, L42, doi: [10.3847/2041-8213/ad63a8](https://doi.org/10.3847/2041-8213/ad63a8)

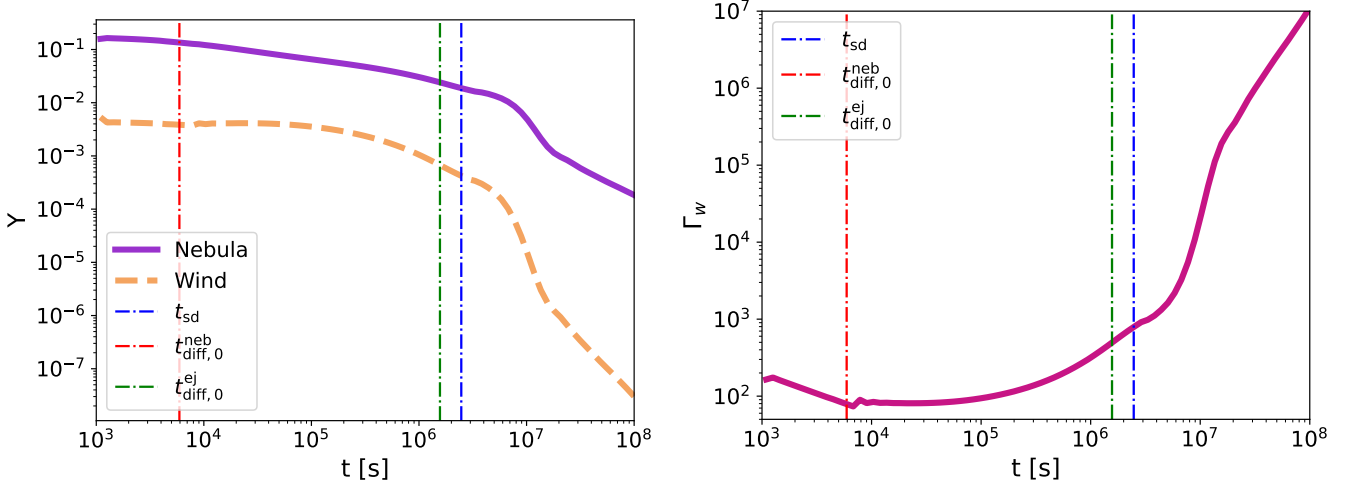


Figure 6. *Left:* Time evolution of pair multiplicity (Y) in the wind and nebula. *Right:* The Lorentz factor of the wind which is also $\gamma_{e,br}$ for the pair injection in the nebula.

APPENDIX

A. PAIRS IN THE WIND AND NEBULA

In this section, we present our calculations for computing the pair multiplicity in the wind and nebular regions and the bulk Lorentz factor in the wind region. The bulk Lorentz factor of the wind primarily governs the break Lorentz factor of the pair injection. The pair multiplicity helps in estimating the diffusion timescale of the photons in the wind and nebula.

A.1. Pair Multiplicity in the nebula

We begin by discussing the prescription to evaluate the pair multiplicity. The pair annihilation rate is determined by $\dot{N}_{e^\pm}^{\text{ann}} = (3/16)\sigma_T c n_\pm N_\pm$, where σ_T is the Thomson cross-section, n_\pm is the number density of pairs, and the total number of pairs is given by $N_\pm = n_\pm V$, V is the volume of the nebula. The pair annihilation timescale $t_{e^\pm}^{\text{ann}}$ can be estimated as, $t_{e^\pm}^{\text{ann}} = 1/((3/16)\sigma_T n_\pm)$. The total number of pairs in the nebula is given by,

$$N_\pm = \begin{cases} \left(\frac{\dot{N}_{e^\pm}^c V}{(3/16)\sigma_T c} \right)^{1/2}, & t_{e^\pm}^{\text{ann}} \leq t_{\text{dyn}} \\ \dot{N}_{e^\pm}^c t_{\text{dyn}}, & t_{e^\pm}^{\text{ann}} > t_{\text{dyn}} \end{cases}, \quad (\text{A1})$$

where the pair creation rate is given by $\dot{N}_{e^\pm}^c$ and t_{dyn} is the dynamical timescale. We compute the pair creation rate by taking into account the pairs created from primary and secondary photons. The pair multiplicity in the nebula is then evaluated as $Y = \dot{N}_{e^\pm}^c m_e c^2 / L_{\text{sd}}$. The first row of the above equation is obtained by balancing the pair creation and annihilation rates, that is, $\dot{N}_{e^\pm}^c = \dot{N}_{e^\pm}^{\text{ann}}$ and solving for the total number of pairs. When the pair annihilation rate is longer than the dynamical timescale, the pairs do not have enough time to annihilate.

In Figure 6 (*left panel*) we show the time evolution of the pair multiplicity. The assumption of $Y = 0.1$ is good for early times but the pair multiplicity drops significantly at late times by an order of magnitude. This happens when $t_{e^\pm}^{\text{ann}} > t_{\text{dyn}}$.

A.2. Lorentz factor of the wind Γ_w

In this subsection, we compute the Lorentz factor associated with the wind. The ultra-relativistic wind is slowed down by the ejecta which then thermalizes to form the termination shock (TS). We denote the radial distance of the wind TS from the central engine as R_s and the bulk Lorentz factor of the wind is denoted as Γ_w .

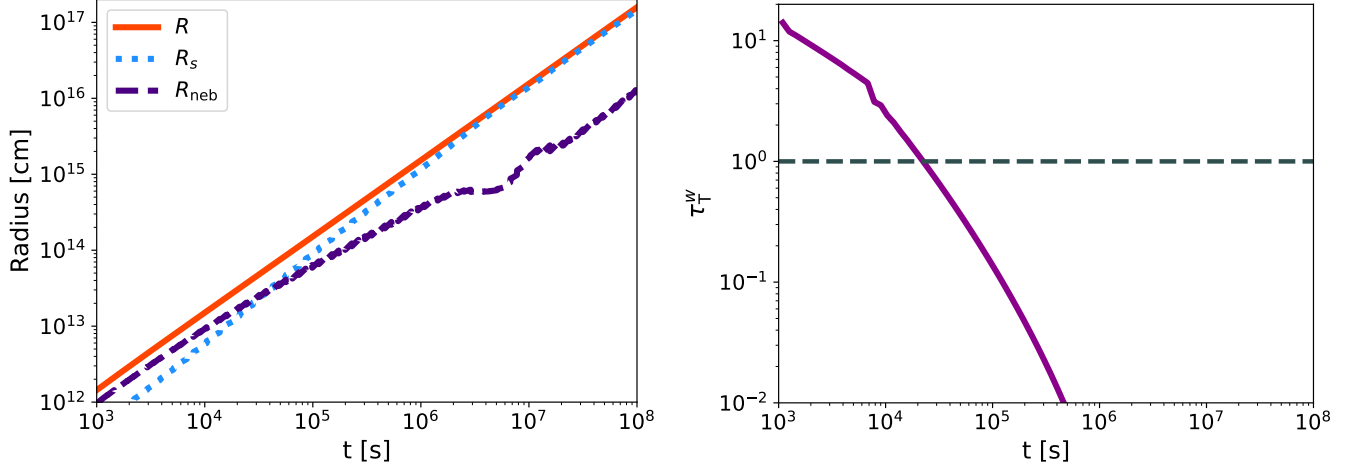


Figure 7. *Left:* Time evolution of R_s , R , and the width of the nebula $R - R_s$. *Right:* Time evolution of the Thomson optical depth in the wind region. Note that $\tau_T^w (t \sim t_{sd}) \ll 1$, therefore the TS is collisionless and not radiation mediated at late times.

The rate of energy deposited in the wind can be estimated using $L_w = 4\pi m_e c^2 n_{e^\pm}^w R_s^2 \Gamma_w c$, where $n_{e^\pm}^w$ is the total number density of pairs in the wind region. The spindown energy from the pulsar sources the energy deposition on the wind region such that $L_w \approx L_{sd}$ and thus

$$\Gamma_w = \frac{L_{sd}}{4\pi m_e c^2 n_{e^\pm}^w R_s^2 c}. \quad (\text{A2})$$

The radius of the TS can be estimated by balancing the pressure in the nebula P_{neb} and the ram pressure P_{ram} . Assuming a relativistic gas, the total pressure in the nebula $P_{neb} = E_{neb}^{tot}/(3V)$, where E_{neb}^{tot} is the total energy in the nebula and $V \sim (4/3)\pi(R^3 - R_s^3)$. The total energy in the nebula is composed of the non-thermal, thermal, magnetic energies and the energy due to $e^+ - e^-$ pairs (E_{part}). We thus have, $E_{neb}^{tot} = f_{trap}(t)(E_{nth} + E_{th}) + E_B + E_{part}$, where $f_{trap}(t) = 1/\sqrt{1 + (t/t_{diff}^{neb})^2}$, accounts for the fraction of non-thermal and thermal radiation that is trapped in the nebula. For $t \ll t_{diff}^{neb}$, that is, at the initial stage when typical nebular diffusion timescales are not relevant, the whole radiation is trapped in the nebula. For $t \gg t_{diff}^{neb}$, the fraction falls off as $\sim 1/t$ since nebular diffusion becomes efficient. The particle energy in the nebula can be estimated as $E_{part} = (m_e c^2) \int d\gamma_e dN_e/d\gamma_e$ where $dN_e/d\gamma_e$ is the resulting spectrum after transport of the injected spectrum.

The ram pressure for a cold ultra-relativistic wind can be estimated by $P_{ram} \simeq F_E/c$, where the energy flux $F_E = L_w/(4\pi R_s^2)$. Balancing P_{neb} and P_{ram} we have

$$R_s^3 + \left(\frac{E_{tot}c}{L_w}\right)R_s^2 - R^3 = 0, \quad (\text{A3})$$

We solve the above equation to obtain R_s such that $R_s \in \mathcal{R}$ and $R_s > 0$, shown in Figure 7 (*left*). Next, we evaluate the total number density of pairs in the wind region, that is, $n_{e^\pm}^w = N_{e^\pm}^w/V_w$, where the volume of the wind region $V_w \approx (4/3)\pi R_s^3$ and $N_{e^\pm}^w$ is the total number of pairs in the wind region. We assume that the density of pair creation rate through secondary two photon pair annihilation $\gamma\gamma \rightarrow e^+e^-$, is the same in the wind and the nebular region, that is, $\dot{n}_+^w = \dot{n}_+^{neb}$. This can then be used to estimate the pair creation rate in the wind region as

$$\dot{N}_+^w = \dot{N}_+^{neb} \left(\frac{R_s^3}{R^3 - R_s^3} \right), \quad (\text{A4})$$

where we assume that \dot{N}_+^{neb} is the pair creation rate from the secondary two photon pair annihilation $\gamma\gamma \rightarrow e^+e^-$. Similar to estimating the total number of pairs in the nebula (N_\pm), the total number of pairs in the wind region ($N_{e^\pm}^w$) can be estimated using Equation (A1) where we replace $\dot{N}_{e^\pm}^c$ with \dot{N}_+^{neb} , $t_{e^\pm}^{ann} \approx 1/((3/16)\sigma_T n_{e^\pm}^w)$ and $t_{dyn}^w \approx R_s/c$ and V replaced by V_w . The Thomson optical depth in the wind region can be defined as $\tau_T^w \sim n_{e^\pm}^w \sigma_T R_s$. We show the

time evolution of τ_T^w in Figure 7 (*right*) and note that $\tau_T^w \ll 1$ for $t \gtrsim 10^5$ s. This is crucial for a few assumptions we make in our formalism. Firstly, the assumption $\dot{n}_+^w = \dot{n}_+^{\text{neb}}$ becomes more reasonable for $\tau_T^w \ll 1$, so for the timescales relevant to us the assumption holds quite well. Secondly, for estimating V_w we assume a volume filling factor instead of assuming a relativistic shell with volume swept up as $4\pi R_s^2 c \delta t$. This is also reasonable since the pulsar wind fills a region enclosed by R_s , that is, the region with radius r is filled where, $R_{\text{lc}} < r < R_s$. As a consequence of V_w , the scaling in Equation (A4) is also well-suited for our purpose. Furthermore, since $\tau_T^w \ll 1$ for $t > t_{\text{sd}}$, the TS is collisionless and not radiation mediated. This implies that our model for shock acceleration at the TS is well-suited. But even though the acceleration at TS does play a role in deciding the maximum energy for the CR protons at late times (see Figure 10), the CR protons mostly escape the system and do not produce neutrinos efficiently (see Figure 11).

The bulk Lorentz factor for the wind is shown in the *right* panel of Figure 6. Most importantly, we assume $\Gamma_w = \gamma_{e,\text{br}}$, that is, the bulk Lorentz factor for the wind decides the break in the injected $e^+ - e^-$ spectra. At initial times, $\Gamma_w \sim 100$, while at late times the wind becomes ultra-relativistic with $\Gamma_w \gtrsim 10^6$. This is similar to what was found in I. Vurm & B. D. Metzger (2021) (see Figure 11 there). This is to be expected since at late times the secondary pair creation rate \dot{N}_+^{neb} drops, resulting in inefficient pair loading in the wind and hence a large Γ_w .

B. PHOTONS IN THE NEBULA AND EJECTA

This section focuses on aspects of photons in the nebular and ejecta regions. In particular, we present details about the heating due to the decay of ^{56}Ni leading to injection of MeV gamma rays in the nebula, the nebular photons spectra relevant for neutrino production, and the attenuation factor of the photons in the ejecta.

B.1. Heating due to decay of ^{56}Ni

Nickel (^{56}Ni) with a half life of ~ 10 days decays to cobalt (Co) with a half life of ~ 100 days, which finally decays to iron (Fe), which can have an impact on the opacity relevant for photons. The decay of ^{56}Ni is computed in the quasi-steady state approximation using

$$\begin{aligned} N_{\text{Ni}} &= N_{0,\text{Ni}} \exp(-t/\tau_{\text{Ni}}), \\ N_{\text{Co}} &= N_{0,\text{Co}} + N_{0,\text{Ni}} (1 - \exp(-t/\tau_{\text{Ni}})), \\ N_{\text{Fe}} &= N_{0,\text{Fe}} + N_{\text{Co}} (1 - \exp(-t/\tau_{\text{Co}})), \end{aligned} \quad (\text{B5})$$

where the half-lives of Ni and Co are given by $\tau_{\text{Ni}} = 8.8$ days and $\tau_{\text{Co}} = 111.3$ days respectively. The initial number fractions of Ni, Co, and Fe are given by $N_{0,\text{Ni}}$, $N_{0,\text{Co}}$, and $N_{0,\text{Fe}}$. The decay of ^{56}Ni deposits thermal energy in the ejecta. This is achieved in the following way that the decay of ^{56}Ni produces MeV gamma-rays which subsequently heat up their surrounding electrons through Compton scattering and produce non-thermal electrons in the process. The non-thermal electrons produced, eventually deposit thermal energy in the ejecta as a result of multiple scattering with gamma-ray photons. The rate of the injected energy can be estimated by

$$\begin{aligned} Q_{\text{Ni}}^{\text{heat}} &= f_{\text{therm}} L_{\text{Ni}}^{\text{decay}}, \\ f_{\text{therm}} &= 1 - \exp(-\tau_\gamma), \\ L_{\text{Ni}}^{\text{decay}} &= 10^{43} \text{ erg s}^{-1} \left(6.45 e^{t/\tau_{\text{Ni}}} + 1.45 e^{t/\tau_{\text{Co}}} \right) \left(\frac{M_{\text{Ni}}}{1M_\odot} \right), \end{aligned} \quad (\text{B6})$$

where the luminosity of MeV gamma-rays thermal photons due to the decay of ^{56}Ni is given by $L_{\text{Ni}}^{\text{decay}}$, the fraction of thermalized photons is denoted by f_{therm} . The opacity of these resulting MeV gamma-rays is given by $\kappa_\gamma = 0.05 \text{ cm}^2 g^{-1}$ (note that this is slightly different from the value we use for the ejecta opacity which is $\kappa_{\text{ej}} = 0.1 \text{ cm}^2 g^{-1}$) such that the optical depth $\tau_\gamma = 3M_{\text{ej}}\kappa_\gamma / (4\pi R_{\text{ej}}^2 \Gamma_{\text{ej}}^2)$.

B.2. Nebular photon spectra

In this subsection, we present the photon spectra in the nebula, which would be relevant for the neutrino production in the nebula through $p\gamma$ interactions (see M. Mukhopadhyay & S. S. Kimura 2025 for more details). Moreover, the photon spectra discussed here undergo attenuation in the ejecta (see Section B.3) and result in the observational EM spectra discussed in Section 4.1.

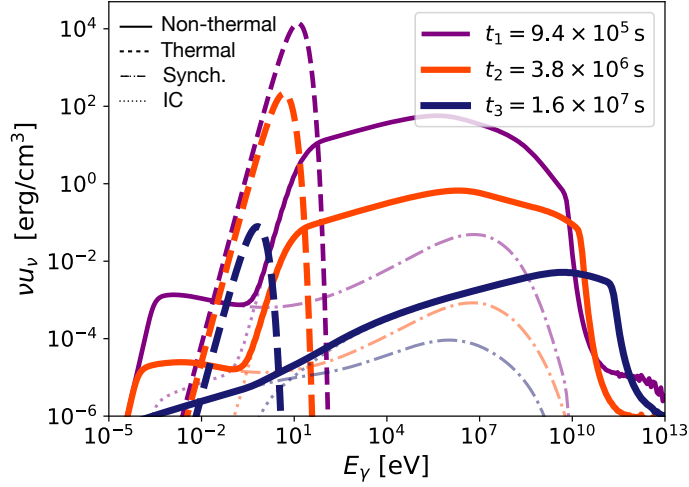


Figure 8. Photon energy density spectrum (νu_ν) of the non-thermal (solid) and thermal (dashed) photons in the nebula (comoving frame) after $\gamma\gamma$ and SSA attenuations, at different timesnaps $t_1 < t_{sd}$, $t_2 \sim t_{sd}$, and $t_3 > t_{sd}$. The corresponding synchrotron (Synch.) and inverse Compton (IC) components are shown with thin dashed-dot and dotted lines respectively.

The distribution of the energy density of non-thermal (solid) and thermal (dashed) photons is shown in Figure 8 for three different timesnaps $t_1 < t_{sd}$ (purple), $t_2 \sim t_{sd}$ (orange), and $t_3 > t_{sd}$ (dark blue). The differential energy density for the thermal photons assuming a blackbody spectrum with temperature $T_{th} \sim (E_{th}/(a_{rad}(4/3)\pi R^3))^{1/4}$ is given by $u_\nu^{th} = (8\pi h\nu^3/c^3)/[\exp(h\nu/(k_B T_{th})) - 1]$, where ν is the frequency, a_{rad} is the radiation constant, E_{th} is the total energy in thermal photons (see Figure 2), and R is the radial distance of the nebula-ejecta boundary. With increase in time post the collapse the peak of the thermal photon energy distribution ($E_{\gamma,th}$) shifts to lower energies. This can be understood by the fact that the thermal temperature decreases with time as a result of decrease in E_{th} (see Figure 2) and increase in the radius of the nebula (see Figure 7, left panel). The thermal temperature for the photons at the timesnaps can be estimated as $T_{th}^{t_1} \approx 4 \times 10^4$ K ($E_{th}^{t_1} \approx 1.4 \times 10^{50}$ erg and $R^{t_1} \approx 1.4 \times 10^{15}$ cm), $T_{th}^{t_2} \approx 1.4 \times 10^4$ K ($E_{th}^{t_2} \approx 7 \times 10^{49}$ erg and $R^{t_2} \approx 5.9 \times 10^{15}$ cm), and $T_{th}^{t_3} \approx 1.9 \times 10^3$ K ($E_{th}^{t_3} \approx 1.6 \times 10^{48}$ erg and $R^{t_3} \approx 2.5 \times 10^{16}$ cm). This implies $E_{\gamma,th}^{t_1} \approx 9.7$ eV, $E_{\gamma,th}^{t_2} \approx 3.4$ eV, and $E_{\gamma,th}^{t_3} \approx 0.47$ eV for t_1 , t_2 , and t_3 respectively. The corresponding peak of the energy density in thermal photon is given by $u_{\nu,th}^{t_1} \approx 1.2 \times 10^4$ erg/cm³, $u_{\nu,th}^{t_2} \approx 1.8 \times 10^2$ erg/cm³, and $u_{\nu,th}^{t_3} \approx 6.4 \times 10^{-2}$ erg/cm³.

The magnetic energy density $u_B \sim \epsilon_B E_{sd}/V$ at the different timesnaps $u_B^{t_1} \approx 2.2$ erg/cm³, $u_B^{t_2} \approx 3.8 \times 10^{-2}$ erg/cm³, and $u_B^{t_3} \approx 2.4 \times 10^{-4}$ erg/cm³. Since $u_B \ll u_{\nu,th}$ (see Figure 2), the non-thermal photon energy density is dominated by inverse Compton (IC), with synchrotron emission contributing at energies lower than $E_{\gamma,th}$ at the relevant time. The peak of the energy density for the non-thermal photon spectra can be estimated using $\nu u_{\nu,IC} = L_{nth}/(4\pi R^2 c)$ such that $\nu u_{\nu,IC}^{t_1} \approx 3.8 \times 10^2$ erg/cm³, $\nu u_{\nu,IC}^{t_2} \approx 6.6$ erg/cm³, and $\nu u_{\nu,IC}^{t_3} \approx 4.2 \times 10^{-2}$ erg/cm³ (note that for t_3 the analytical estimate deviates slightly from the value obtained using numerics because in the late regimes the fast cooling approximation of pairs used in estimating $\nu u_{\nu,IC}$ starts becoming less accurate). The decrease in the peak follows the decrease in L_{nth} as expected. The peak energy of the non-thermal photons can be estimated as $E_{\gamma,nth} \sim \gamma_{e,br}^2 E_{\gamma,th}$. As seen from the figure peak shifts to higher energies with time since $E_{\gamma,nth}^{t_1} \approx 8.7 \times 10^5$ eV ($\gamma_{e,br}^{t_1} \sim 300$), $E_{\gamma,nth}^{t_2} \approx 4.16 \times 10^6$ eV ($\gamma_{e,br}^{t_2} \sim 1100$), and $E_{\gamma,nth}^{t_3} \approx 1.9 \times 10^{10}$ eV ($\gamma_{e,br}^{t_3} \sim 2 \times 10^5$).

At high-energies the photon spectra is suppressed by Klein-Nishina (KN) and $\gamma\gamma$ attenuation. The former can be estimated using $E_{\gamma,KN} = \gamma_{e,KN}^2 E_{\gamma,th}$, where $\gamma_{e,KN} \gtrsim (m_e c^2)/E_{\gamma,th}$. Thus for the timesnaps t_1 , t_2 , and t_3 the KN suppression becomes relevant for $E_{\gamma,KN}^{t_1} \approx 2.7 \times 10^{10}$ eV, $E_{\gamma,KN}^{t_2} \approx 7.7 \times 10^{10}$ eV, and $E_{\gamma,KN}^{t_3} \approx 5.6 \times 10^{11}$ eV respectively. For $\gamma\gamma$ cutoff above $E_{\gamma,th}$ the target photon energy, in this case the energy in thermal photons decreases rapidly. In this scenario, the $\gamma\gamma$ cutoff can be estimated using $E_{\gamma\gamma,cut} \approx (m_e c^2)/E_{\gamma,th} \approx E_{\gamma,KN}$.

B.3. Attenuation in the nebula and ejecta

In this subsection we discuss the attenuation of the photon spectra in the nebula due to SSA and $\gamma\gamma$ processes, followed by the attenuation in the ejecta across all wavelengths due to free-free, bound-bound, bound-free, Compton

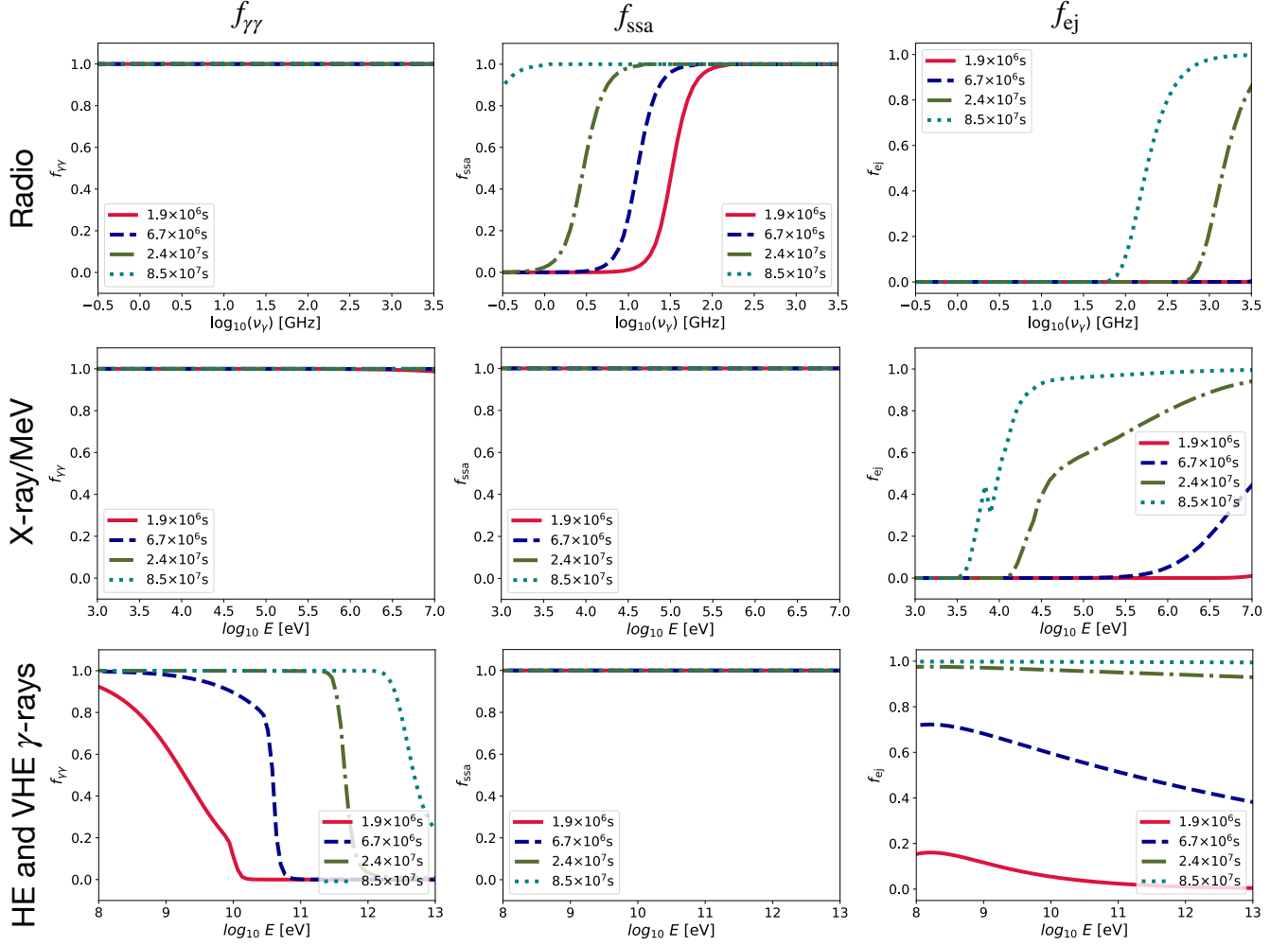


Figure 9. Attenuation coefficients at different time snaps for $\gamma\gamma$, SSA, and ejecta attenuations denoted by $f_{\gamma\gamma}$, f_{SSA} , and f_{ej} respectively. The plots are shown for radio, X-ray/MeV, and high energy (HE) and very high energy (VHE) gamma-rays. The value of $f = 1$ corresponds to $\tau = 0$.

and Bethe-Heitler processes (see [M. Mukhopadhyay & S. S. Kimura 2025](#) for additional details). The observed EM spectra shown in [Figure 3](#) is a result of the attenuation of the photons in the nebula and the ejecta regions.

The attenuation factors are defined in the following way $f_{\gamma\gamma} = (1 - e^{-\tau_{\gamma\gamma}})/\tau_{\gamma\gamma}$, $f_{\text{SSA}} = (1 - e^{-\tau_{\text{SSA}}})/\tau_{\text{SSA}}$, and $f_{\text{ej}} = e^{-\tau_{\text{ej}}}$, where $f \rightarrow 1$ corresponds to optical depth $\tau \rightarrow 0$. The attenuation factors across the radio, X-ray/MeV, and high-energy (HE) and very HE gamma-rays are shown in [Figure 9](#) for different timesnaps. For the radio band the SSA optical depth and the free-free absorption in the ejecta highly suppress the emission. X-ray/MeV photons are suppressed mostly by the bound-free opacity of ejecta. Since the bound-free opacity is higher for lower energies, the ejecta becomes transparent to X-ray photons later than the MeV photons, explaining the rise of the MeV photon spectra at earlier times than the X-ray photon spectra. The MeV photons are scattered and reprocessed to lower energies through Compton scattering, which serves as the dominant attenuation channel.

Gamma-rays at GeV and TeV energies are mostly suppressed by the $\gamma\gamma$ attenuation in the nebula followed by Bethe-Heitler attenuation in the ejecta. The GeV photon spectra is observed earlier than the TeV photons because the $\gamma\gamma$ optical depth increases with increase in E_γ . Thus, even though the ejecta becomes transparent to GeV photons at $t \sim 10^7$ s post collapse, the $\gamma\gamma$ suppression completely suppresses TeV emission until very late times $t \sim 2.4 \times 10^7$ s.

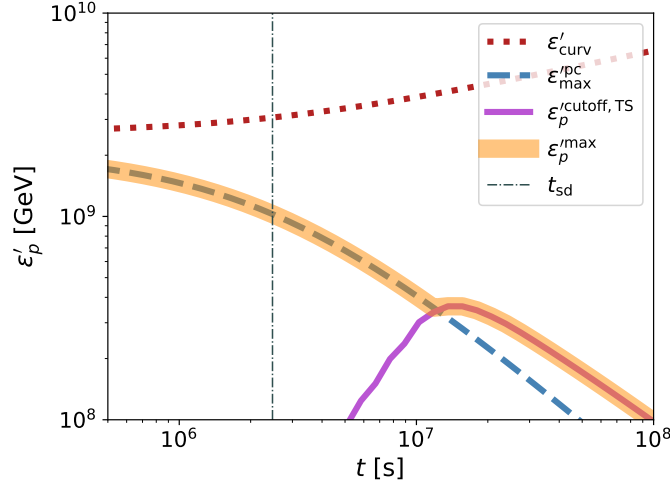


Figure 10. Time evolution of the relevant CR proton energies in different regions: the maximum energy that the protons can be accelerated to in the polar cap and TS regions are denoted by $\varepsilon_{\text{max}}^{\text{pc}}$ (Equation C8) and $\varepsilon_p^{\text{cutoff,TS}}$ respectively, the proton energy limited by curvature losses in the polar cap region is denoted by $\varepsilon'_{\text{curv}}$ (Equation C7). The cut-off energy for the CR protons in a SLSNe ($\varepsilon_p^{\text{max}}$) is shown as a shaded orange-yellow band.

C. HADRONIC PROCESSES IN THE NEBULA

This section summarizes the hadronic processes in the nebula. In particular, the maximum energy achievable by the CR proton as a result of acceleration in the polar cap and TS regions and the associated timescales for acceleration and energy loss.

C.1. Maximum CR proton energies

In this subsection we focus on evaluating the maximum energy to which CR protons can be accelerated in a millisecond magnetar powered SLSNe. We refer the reader to [M. Mukhopadhyay et al. \(2025\)](#) (see Section 4 there) for a detailed discussion of the relevant energies and briefly discuss the results. Recall that in our setup there are two sites of particle acceleration – the polar cap region of the magnetar and the termination shock (TS).

The maximum energy to which protons can be accelerated in the polar cap region $\varepsilon_{\text{max}}^{\text{pc}}$ (dashed light blue), the energy cut off due to curvature losses $\varepsilon'_{\text{curv}}$ (dotted maroon), the maximum energy that protons can be accelerated to in the TS region $\varepsilon_p^{\text{cutoff,TS}}$ (solid light purple), and the maximum energy that the CR protons can be accelerated to $\varepsilon_p^{\text{max}}$ (shaded orange-yellow band) are shown as a functions of time post collapse in Figure 10. We notice that given the choice of our fiducial parameters the acceleration across TS governs $\varepsilon_p^{\text{max}}$ at late times $t > 10^7$ s. However, at such late times neutrino production is not efficient since the protons mostly escape from the nebula as evident from Figure 11 (*right panel*).

The curvature energy loss can be defined in the following way

$$\varepsilon'_{\text{curv}} = \gamma_p m_p c^2 = \left[\frac{3m_p^4 c^8 B_d R_{\text{curv}}^2}{2Ze} \right]^{1/4} = 2.6 \times 10^9 \text{ GeV} \left(\frac{B_d}{5 \times 10^{13} \text{ G}} \right)^{1/4} \left(\frac{Z}{1} \right)^{-1/4} \left(\frac{P_i}{4 \text{ ms}} \right)^{1/2} \left(1 + \frac{t}{t_{\text{sd}}} \right)^{1/4}, \quad (\text{C7})$$

where γ_p is the Lorentz factor of the protons and R_{curv} is the radius of curvature, which we assume to be $R_{\text{lc}} = c/\Omega$, $\Omega = 2\pi/P$ is the angular velocity and the spin period $P(t) = P_i(1 + t/t_{\text{sd}})^{1/2}$. This implies that for $t \ll t_{\text{sd}}$, $\varepsilon'_{\text{curv}}$ is roughly constant and for $t \gg t_{\text{sd}}$ it increases as $\sim t^{1/4}$. The acceleration of protons in the potential gap created in the polar cap region can be estimated as¹¹

$$\varepsilon_{\text{max}}^{\text{pc}} = 2\eta_{\text{gap}}(Ze)B_d \left(\frac{\pi R_*}{cP} \right)^2 R_* = 2 \times 10^9 \text{ GeV} \left(\frac{\eta_{\text{gap}}}{0.1} \right) \left(\frac{B_d}{5 \times 10^{13} \text{ G}} \right) \left(\frac{Z}{1} \right) \left(\frac{R_*}{10 \text{ km}} \right) \left(\frac{P_i}{4 \text{ ms}} \right)^{-2} \left(1 + \frac{t}{t_{\text{sd}}} \right)^{-1}, \quad (\text{C8})$$

¹¹ Note the factor in front should be 2 instead of 4, which was a typo in our previous work [M. Mukhopadhyay et al. \(2025\)](#). This is because we define the magnetic dipole moment of the magnetar as $\mu = B_d R_*^3$ instead of $B_d R_*^3/2$ used in the literature. Thus the potential gap created $\Phi_{\text{mag}} = \Omega^2 \mu / c^2$.

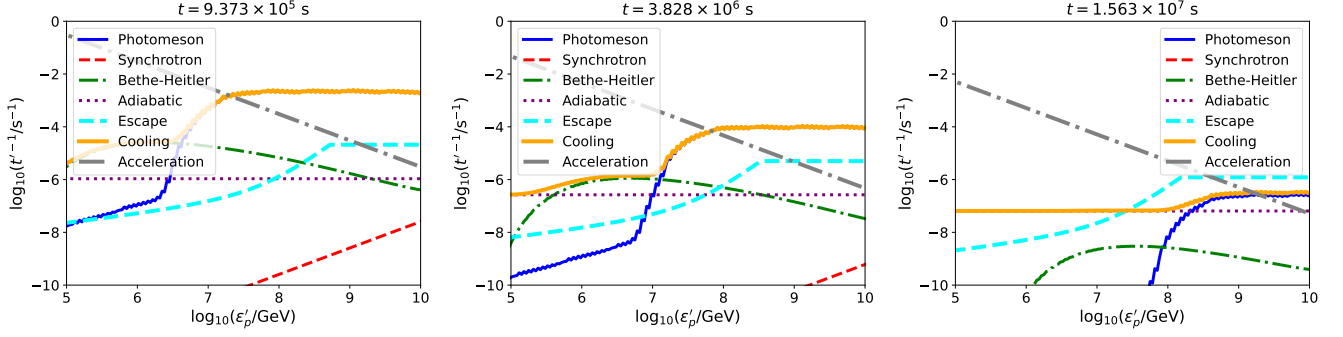


Figure 11. Plots showing the rates of various acceleration and cooling processes with comoving proton energy ε'_p at various timesnaps.

where η_{gap} is the fraction of the total potential difference experienced by the charged particle. We use $\sim 10\%$ of the potential gap which can be reasonable due to screening effects from the surrounding plasma. For $t > t_{\text{sd}}$, $\varepsilon_{\text{max}}^{\text{pc}}$ falls off as t^{-1} and therefore, $\varepsilon_p^{\text{max}}$ is limited by $\varepsilon_{\text{max}}^{\text{pc}}$ for late times.

The maximum CR proton energy in the TS region is evaluated by balancing the acceleration timescale t'_{acc} with the loss timescale t'_{loss} . We discuss and show the various different timescales in the following section.

C.2. CR proton timescales for neutrino emission

In this subsection we briefly discuss the relevant acceleration and loss timescales for the CR protons which are play a role in governing the the maximum energy of protons in the TS region and the efficiency of neutrino production. A more detailed description for the timescales can be found in [M. Mukhopadhyay et al. \(2025\)](#) (see Section 4.3 there).

The acceleration timescale for the protons in the TS region can be estimated as $t'_{\text{acc}} \sim \eta_{\text{acc}} \varepsilon'_p / (ecB'_{\text{neb}})$, where the comoving magnetic field in the nebula $B'_{\text{neb}} \approx \sqrt{2}(E_B / (R^2 v_{\text{ej}} t))$ and we choose the acceleration efficiency $\eta_{\text{acc}} \sim 1$. The rate of energy loss for the protons is determined by their rate of escape (t'^{-1}_{esc}) through diffusion or free-streaming and their rate of cooling (t'^{-1}_{cool}). Furthermore, the cooling rate for the protons includes contributions from pp , $p\gamma$, synchrotron, inverse Compton, Bethe-Heitler, and dynamical processes. In [Figure 11](#) we show the rate of proton acceleration (t'^{-1}_{acc}) (dot-dashed gray), cooling (t'^{-1}_{cool}) (solid yellow) including the various channels, and escape (t'^{-1}_{esc}) as a function of their comoving energy for different instances in time. Since the peak of neutrino emission occurs between $10^6 - 10^{6.5}$ s, we have chosen the timesnaps accordingly.

For $t < t_{\text{sd}}$ (*left* panel), protons with energy $\varepsilon'_p \gtrsim 10^7$ GeV efficiently cool through $p\gamma$ interactions while $\varepsilon'_p < 10^7$ GeV are cooled through BH processes. For $t \sim t_{\text{sd}}$ (*middle* panel), protons are accelerated efficiently upto $\varepsilon'_p \lesssim 10^8$ GeV (however the maximum proton energy is still governed by the polar cap acceleration, see [Figure 10](#)) and they efficiently cool through $p\gamma$ interactions. Furthermore, in this regime escape timescales are longer implying the $p\gamma$ cooling ideal for neutrino production through pions are efficient. Indeed we see that the neutrino fluence peaks around $t_{\text{sd}} \sim 10^6 - 10^{6.5}$ s with the peak neutrino energy between $10^7 - 10^8$ GeV. The target photons relevant for neutrino production in this regime have energies $\sim 3 - 30$ eV. Given the thermal photons around t_{sd} have energy $E_{\gamma, \text{th}}^{t_{\text{sd}}} \sim 3.4$ eV, which implies that the thermal photons serve as the main target for neutrino production. At late times $t \gg t_{\text{sd}}$ (*right* panel) protons with energy $\varepsilon'_p > 3 \times 10^7$ GeV efficiently escape leading to a sharp decline in the neutrino production rate.

D. NEUTRINO STACKING SEARCHES USING EM TELESCOPES

In this section we present the relevant details for evaluating prospects of stacking searches in the current and upcoming neutrino telescopes using optical observations of SLSNe in Rubin/Roman. The detection significance obtained as a result is shown in [Figure 5](#) (*right*) for different neutrino telescopes.

D.1. Rate of SLSNe

The redshift-dependent volumetric rate density of SLSNe is given by $\dot{\rho}(z) = \dot{\rho}_0(\psi_z/\psi_0)$, where $\dot{\rho}_0$ is the fiducial volumetric rate density at redshift $z = 0$, ψ_z gives the evolution of the star formation rate with z , and $\psi_0 = \psi_{z=0}$. We assume $\dot{\rho}_0 = 10^{-7} \text{ Mpc}^{-3} \text{ yr}^{-1}$ and ψ_z is given by [M. Mukhopadhyay & S. S. Kimura \(2026\)](#) (see Equation C4 there).

Thus in a redshift bin dz the observed SLSNe rate is given by

$$\frac{d\dot{N}}{dz} = \frac{dV_{\text{com}}}{dz} \frac{\dot{\rho}(z)}{(1+z)} = 4\pi \frac{c d_{\text{com}}^2(z)}{H(z)} \frac{\dot{\rho}(z)}{(1+z)}, \quad (\text{D9})$$

where the all-sky comoving volume element is given by $dV_{\text{com}}/dz = 4\pi dV_{\text{com}}/(dz d\Omega)$ and we assume flat spacetime to obtain the simplification in the second equality, the redshift evolution of the Hubble expansion rate for flat Λ CDM cosmology is $H(z) = H_0 \sqrt{\Omega_m(1+z)^3 + \Omega_\Lambda}$, where the matter and vacuum energy density fraction is given by $\Omega_m = 0.3$ and $\Omega_\Lambda = 0.7$ respectively. The comoving distance d_{com} is related to the luminosity distance d_L using $d_L = (1+z)d_{\text{com}}$. It is easy to see from above that the total number of SLSNe given a maximum redshift z_{max} and an observation time T_{obs} can be evaluated using $N_{\text{SLSNe}}(T_{\text{obs}}, z_{\text{max}}) = T_{\text{obs}} \int_0^{z_{\text{max}}} dz (d\dot{N}/dz)$, where we have for $T_{\text{obs}} = 10$ years and $z_{\text{max}} = 1$, $N_{\text{SLSNe}} \approx 4 \times 10^5$.

D.2. Neutrino signal events from a population of SLSNe

The observed differential neutrino number flux from a SLSNe at luminosity distance d_L is defined as

$$\phi_\nu^{\text{obs}}(z, t^{\text{obs}}, E_\nu^{\text{obs}}) = \frac{\phi_\nu^{\text{src}}}{4\pi d_L(z)^2} = \frac{1}{4\pi d_L(z)^2} \left(\frac{d^2 \dot{N}_\nu^{\text{src}}}{dE_\nu^{\text{src}} dt^{\text{src}}} \right) \quad (\text{D10})$$

where the rate of neutrino production at the SLSNe (source) is given by ϕ_ν^{src} and is defined as term in the parenthesis in the second equality above. The source and observer frame neutrino energy is given by E_ν^{src} and E_ν^{obs} respectively, such that $E_\nu^{\text{src}} = (1+z)E_\nu^{\text{obs}}$. Similarly the source frame and the observer frame time interval is related by $dt^{\text{obs}} = (1+z)dt^{\text{src}}$. Using Equation (D10), the time-integrated observed neutrino number fluence is defined as

$$J_\nu^{\text{obs}}(z, E_\nu^{\text{obs}}) = \int dt^{\text{obs}} \phi_\nu^{\text{obs}}(z, t^{\text{obs}}, E_\nu^{\text{obs}}) = \frac{(1+z)}{4\pi d_L(z)^2} \int_{t_{\text{min}}^{\text{src}}}^{t_{\text{max}}^{\text{src}}} dt^{\text{src}} \left(\frac{d^2 \dot{N}_\nu^{\text{src}}}{dE_\nu^{\text{src}} dt^{\text{src}}} \right) \Bigg|_{E_\nu^{\text{src}}=(1+z)E_\nu^{\text{obs}}}. \quad (\text{D11})$$

For a nearby source like a SLSNe at $d_L = 100$ Mpc, we can assume that the redshift $z \approx 0$ which simplifies the above expression and allows us to drop the superscripts. Hence in Figure 5 (left) we show $E_\nu^2 J_\nu$ as the neutrino fluence from a SLSNe at 100 Mpc ignoring the superscripts. We also choose $t_{\text{min}}^{\text{src}}$ and $t_{\text{max}}^{\text{src}}$ as half-decades in time from 10^5 s to $10^{7.5}$ s to show the time-integrated neutrino fluences. The all-flavor effective areas ($A_{\text{eff}}(E_\nu)$) for RNO-G, IceCube-Gen2 Radio, GRAND, and BEACON are obtained from K. Kotera et al. (2026) (see Figure 2 upper panel and references therein). Additionally, we also consider KM3NeT (S. Adrian-Martinez et al. 2016), a typical 10 km^3 telescope in the form of HUNT (M. Chen 2026) or TRIDENT (Z. P. Ye et al. 2023), and NEON (H. Zhang et al. 2025). Given that both HUNT and TRIDENT will be water-based and have similar characteristics to KM3NeT, we use the KM3NeT effective area scaled by the detector volume ($\sim 10^{2/3}$) as an approximation for HUNT's and TRIDENT's effective area.

Since the neutrino emission from SLSNe peak roughly a few 10 days post the collapse, the instantaneous effective area is not suitable and hence the day-averaged effective area needs to be used. While using the day-averaged effective area it is important to include the field of view (FOV) of the relevant detector since the day-averaged FOV is different from the instantaneous FOV for detectors not at the Pole. In our analysis, we consistently use the day-averaged effective area including the FOV. For IceCube we choose the all-flavor effective areas corresponding to the high-energy starting events (HESE) (R. Abbasi et al. 2021). This choice is reasonable since the typical neutrino energy from SLSNe have $E_\nu > 10^5$ GeV. Finally, for IceCube-Gen2 we scale the effective area used for IceCube by a factor of $10^{2/3}$ due to the volume scaling of Gen2 with regards to current IceCube.

The total number of detected neutrino signal events from a single SLSNe at a redshift z can be computed as $N_{\text{sig}}(z) = \int dE_\nu^{\text{obs}} J_\nu^{\text{obs}}(z, E_\nu^{\text{obs}}) A_{\text{eff}}(E_\nu^{\text{obs}})$. With all the ingredients discussed above (Equations D9 and D11), the total number of stacked neutrino signal events that can be obtained from all SLSNe within a maximum redshift z_{max} and observation time T_{obs} is defined as

$$N_{\text{sig}}^{\text{tot}}(T_{\text{obs}}, z_{\text{max}}) = T_{\text{obs}} \int_0^{z_{\text{max}}} dz \frac{d\dot{N}}{dz} \int_{E_\nu^{\text{min}}}^{E_\nu^{\text{max}}} dE_\nu^{\text{obs}} J_\nu^{\text{obs}}(z, E_\nu^{\text{obs}}) A_{\text{eff}}(E_\nu^{\text{obs}}). \quad (\text{D12})$$

We choose the maximum redshift as $z_{\text{max}} = 1$. This is typical of current and upcoming surveys like Rubin LSST, which can easily observe SLSNe for $z \sim 1$. Note that increasing z does not necessarily guarantee an increase in the

detection significance since increasing z leads to an increase in $N_{\text{tot}}^{\text{bkg}}$ (Equation D13) since N_{SLSNe} increases but $N_{\text{tot}}^{\text{sig}}$ may not increase comparatively since the contribution from far away sources become lesser as $d_L(z)$ increases. As evident from Figure 5 (left), the high energy neutrinos from SLSNe peak for $E_\nu > 10^5$ GeV, so we choose E_ν^{min} and E_ν^{max} as 10^5 GeV and 10^{12} GeV respectively. This greatly helps in reducing atmospheric backgrounds.

D.3. Background events

The diffuse astrophysical neutrino flux that would serve as background is uncertain for $E_\nu > 10^6$ GeV. However, we provide an estimate of backgrounds by considering the latest background flux template from IceCube. In a stacking search the neutrino detector will also collect background events besides collecting signal events. We consider conventional, prompt, and astrophysical backgrounds for this work, that is, $\phi_\nu^{\text{bkg,obs}}(E_\nu) = \phi_\nu^{\text{bkg,conv}} + \phi_\nu^{\text{bkg,prompt}} + \phi_\nu^{\text{bkg,astro}}$. We estimate the conventional atmospheric neutrino flux using the model described in M. Honda et al. (2007), while the prompt atmospheric background is estimated from R. Enberg et al. (2008). The diffuse astrophysical background is estimated using the broken power-law fit to the IceCube data (R. Abbasi et al. 2024). This gives the diffuse isotropic astrophysical flux as $\phi_\nu^{\text{bkg,astro}}(E_\nu) = \phi_0 (E_{\text{break}}/100 \text{ TeV})^{-\gamma_2} (E_\nu/E_{\text{break}})^{-\gamma_2}$, where the all-flavor normalization $\phi_0 = 5.1 \times 10^{-17} \text{ GeV}^{-1} \text{cm}^{-2} \text{s}^{-1} \text{sr}^{-1}$, the spectral index $\gamma_2 = 2.52$, and the energy break $E_{\text{break}} = 22.9$ TeV. Note that we just use the $E_\nu > E_{\text{break}}$ branch of the broken power law since the SLSNe neutrino emission is dominated by neutrino energies $> 10^5$ GeV. It is important to note that the IceCube analysis is dominated by neutrino flux below 100 TeV. The extrapolation to $E_\nu > 10^7$ is optimistic since there could be additional astrophysical sources at higher energies. Given we work with energies of 100 TeV and above, even though we consider the atmospheric fluxes, the background for $E_\nu > 10^5$ GeV is completely dominated by the astrophysical background, such that, $\phi_\nu^{\text{bkg,obs}}(E_\nu) = \phi_\nu^{\text{bkg,astro}}(E_\nu)$.

Any SLSNe detected by an EM telescope, that is subsequently used for performing a stacking search to look for neutrino events will contribute to the number of background events N_{bkg} that is collected. Given the isotropic background rate, the contribution will depend on the angular error associated ($\Delta\Omega_{\text{err}}$) and the time window across which the search is performed (δt_{search}). The former depends on the error associated with the localization of the source given the EM and neutrino detectors, that is, $\Delta\Omega_{\text{err}} = \max[\Delta\Omega_{\text{err}}^{\text{EM}}, \Delta\Omega_{\text{err}}^\nu]$, while the latter depends on when the neutrino emission from the source in this case SLSNe peaks, that is, what would be the optimal time-window for the search. In general $\Delta\Omega_{\text{err}}^{\text{EM}}$ is independent of distance to the source while $\Delta\Omega_{\text{err}}^\nu$ depends on the topology of the neutrino event in the detectors like tracks versus cascades. However, for EM telescopes, typical source localizations are at the level of arcseconds compared to a few degree localization from the neutrino telescopes, that is, $\Delta\Omega_{\text{err}}^{\text{EM}} \ll \Delta\Omega_{\text{err}}^\nu$ and thus we can assume $\Delta\Omega_{\text{err}} \approx \Delta\Omega_{\text{err}}^\nu$. Thus for any observed SLSNe used for stacking, the corresponding background accumulated is $N_{\text{bkg}} = \delta t_{\text{search}} \Delta\Omega_{\text{err}} \int dE_\nu^{\text{obs}} \phi_\nu^{\text{bkg,obs}}(E_\nu^{\text{obs}}) A_{\text{eff}}(E_\nu^{\text{obs}})$. Note that the smaller the values of $\Delta\Omega_{\text{err}}$ and δt_{search} , the lower the accumulated backgrounds in stacking searches. Similar to Equation (D12), the total number of background neutrino events accumulated as a result of the stacking search can be defined as

$$N_{\text{bkg}}^{\text{tot}}(T_{\text{obs}}, z_{\text{max}}) = N_{\text{SLSNe}} N_{\text{bkg}} = T_{\text{obs}} \left(\int_0^{z_{\text{max}}} dz \frac{d\dot{N}}{dz} \right) \left(\delta t_{\text{search}} \Delta\Omega_{\text{err}} \int_{E_\nu^{\text{min}}}^{E_\nu^{\text{max}}} dE_\nu^{\text{obs}} \phi_\nu^{\text{bkg,obs}}(E_\nu^{\text{obs}}) A_{\text{eff}}(E_\nu^{\text{obs}}) \right). \quad (\text{D13})$$

Note that since $\phi_\nu^{\text{bkg,obs}}$ is independent of the redshift, the two integrals separate out. Furthermore, given the neutrino emission peaks for $t \sim 10^6 - 10^7$ s, we choose the optimal time-window for search as $\delta t_{\text{search}} \sim 10^{6.4} \text{ s} \approx 30$ days. The assumption we make here is that all samples in our catalog of SLSNe for the stacking search has neutrino emission characteristics similar to our fiducial case. This can be improved by considering a scan over the parameter space to get a slightly more realistic estimate. Lastly, we choose the angular error for in-ice detectors like IceCube and IceCube-Gen2 to be $\theta_{\text{err}}^{\nu,\text{ice}} \sim 1^\circ$ while that for the radio neutrino detectors to be $\theta_{\text{err}}^{\nu,\text{rad}} \sim 0.5^\circ$, and water-based detectors $\theta_{\text{err}}^{\nu,\text{water}} \sim 0.25^\circ$ which gives $\Delta\Omega_{\text{err}}^{\nu,\text{ice}} = 2\pi(1 - \cos\theta_{\text{err}}^{\nu,\text{ice}}) \approx 10^{-3}$ sr, $\Delta\Omega_{\text{err}}^{\nu,\text{ice}} \approx 2 \times 10^{-4}$ sr, and $\Delta\Omega_{\text{err}}^{\nu,\text{water}} \approx 6 \times 10^{-5}$ sr respectively. This is reasonable since in-ice detectors indeed have slightly poor angular resolution than air shower detectors, while water-based detectors have excellent angular resolutions.

With these assumptions and choosing $z_{\text{max}} = 1$ and $T_{\text{obs}} = 10$ years, we find the background rate in a typical radio detector like IceCube-Gen2 Radio would be $\sim 3 \text{ yr}^{-1}$. The detection significance in the Gaussian limit can be defined as

$$\sigma_{\text{det}}(T_{\text{obs}}, z_{\text{max}}) = \frac{N_{\text{sig}}^{\text{tot}}}{\sqrt{N_{\text{sig}}^{\text{tot}} + N_{\text{bkg}}^{\text{tot}}}}, \quad (\text{D14})$$

where $N_{\text{sig}}^{\text{tot}}$ and $N_{\text{bkg}}^{\text{tot}}$ are given by Equations (D12) and (D13) respectively. We show the detection significance for various current, upcoming, and proposed ice, air, and water based detectors neutrino detectors in Figure 5 (*right*).